Solid-State Thermal Control Devices

Timm Swoboda, Katja Klinar, Ananth Saran Yalamarthy, Andrej Kitanovski, and Miguel Muñoz Rojo*

Over the past decade, solid-state thermal control devices have emerged as potential candidates for enhanced thermal management and storage. They distinguish themselves from traditional passive thermal management devices in that their thermal properties have sharp, nonlinear dependencies on direction and operating temperature, and can lead to more efficient circuits and energy conversion systems than what is possible today. They also distinguish themselves from traditional active thermal management devices (e.g., fans) in that they have no moving parts and are compact and reliable. In this article, the recent progress in the four broad categories of solid-state thermal control devices that are under active research is reviewed: diodes, switches, regulators, and transistors. For each class of device, the operation principle, material choices, as well as metrics to compare and contrast performance are discussed. New architectures that are explored theoretically, but not experimentally demonstrated, are also discussed.

1. Introduction

In this review, we present the most recent advances in the field of solid-state thermal control devices, with special emphasis on thermal diodes, regulators, switches, and transistors.[1–4] These thermal devices are made of materials that exhibit nonlinear and switchable thermal behavior.[2] Their fundamental difference compared to fluidic or mechanical thermal devices relies on the fact that they do not have moving parts or fluids.[5] Thus, solid-state thermal devices are silent, reliable, and can be easily scaled down.[5,6] This makes them ideal for thermal management of batteries[7] and electronics,[8] or the development

of novel thermal technologies such as phonon logic.[9–11] On the other hand, the performance of solid-state thermal devices achieved so far are typically lower than the ones obtained by mechanical or fluidic devices.[12] Nevertheless, solid-state devices have plenty of room for improvement because of their high degree of material tunability (size,[13–18] shape,[19,20] physical-chemistry,[21] etc.). In recent years, there has been substantial interest in solid-state thermal devices due to their potential for active thermal control.[14] This has led to an increasing number of experimental and theoretical advances in this field where new structures and materials are studied to improve our thermal management capabilities.[14]

This review is divided into four main sections, which are illustrated in **Figure 1**. First, in Section 2, we present solid-state thermal diodes. We explain the approaches carried out to obtain thermal rectification. Second, in Section 3, we introduce solid-state thermal switches. We organized this section based on the external parameters that induce thermal switching, such as magnetic or electric fields, pressure, or light. Third, in Section 4, we explain solid-state thermal regulators and their recent advances. Finally, in Section 5, we review the solid-state thermal transistors that have been reported to date, focusing mainly on electrochemical transistors. In all these sections, we provide information about the key parameters that determine the performance of the thermal control devices, like rectification ratios (RR), switching ratios (SR), or the characteristic switching times τ, among others. Additionally, theoretical predictions on promising thermal devices are presented in each section. They represent new opportunities in the field, showing new material approaches[22,23] or suggestions for improving existing devices.[24] In Section 6, we discuss the future progress of thermal control devices.

2. Thermal Diodes

Solid-state thermal diodes present an asymmetric heat flow that depends on the direction of the temperature gradient, i.e., forward (fwd) versus reverse (rev) direction.[25] This is typically achieved by material engineering[26] or by connecting materials (junction) with dissimilar thermal properties.[1] The research of solid-state thermal diodes started when Starr[27] showed thermal

T. Swoboda, Dr. M. Muñoz Rojo
Department of Thermal and Fluid Engineering
University of Twente
Enschede, AE 7500, The Netherlands
E-mail: m.munozrojo@utwente.nl
K. Klinar, Prof. A. Kitanovski
Faculty of Mechanical Engineering
University of Ljubljana
Akserceva 6, Ljubljana 1000, Slovenia
Dr. A. S. Yalamarthy[+]
Department of Mechanical Engineering
Stanford University
Stanford, CA 94305, USA

The ORCID identification number(s) for the author(s) of this article can be found under https://doi.org/10.1002/aelm.202000625.

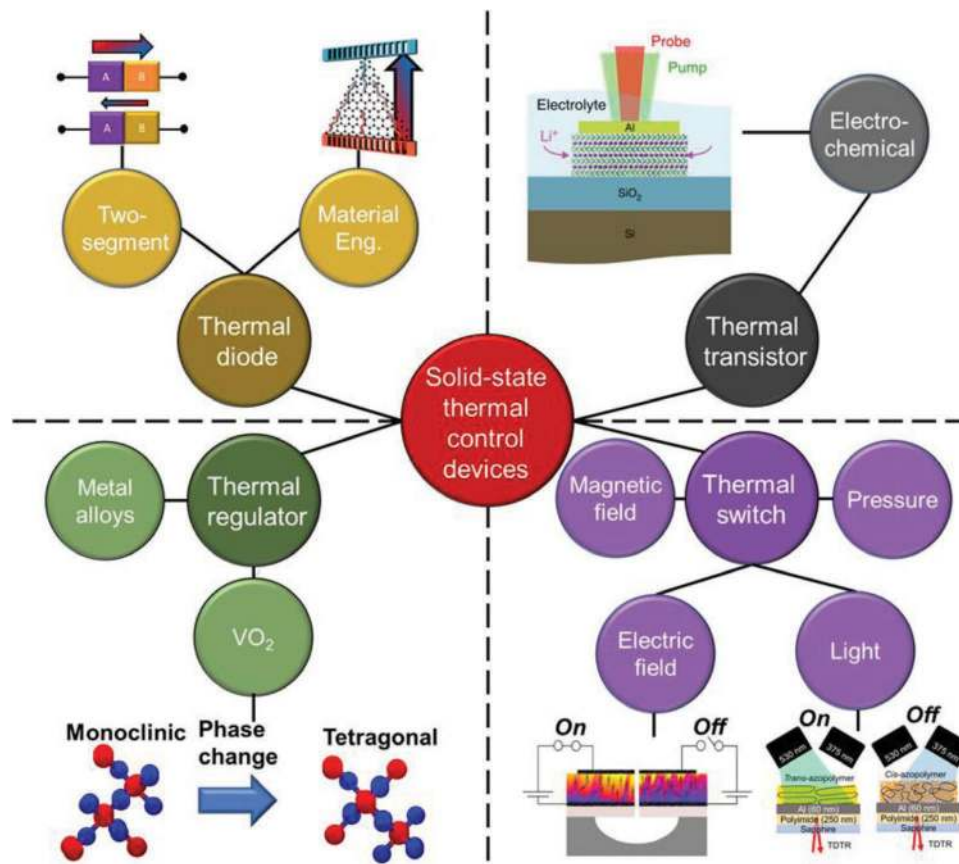[+]Present address: Frore Systems Inc., San Jose, CA 95131, USA

Figure 1. Solid-state thermal control devices.

rectification in copper oxides in 1936. More recently, nanotechnology has brought new material engineering opportunities to design reliable and efficient thermal rectifiers.[28] The development of these devices has shown promising features for better management of heat in electronics,[29–32] electrocaloric refrigeration,[2] or for thermal computing.[11]

In Section 2, given the new opportunities that nanotechnology has brought with regards to material engineering and miniaturization,[26] we focus mainly on nano to microscale thermal diodes. In this context, two engineering processes, can be used to develop solid-state thermal diodes: i) combination of different materials, i.e., two-segment materials[33] (Section 2.1) or ii) modification of the shape or size of the devices, i.e., material engineered structures[34] (Section 2.2). The different architectures can be compared using the following parameters, which are key to determine the performance of thermal diodes:

i. *Rectification ratio*: Corresponds to the ability of the device to rectify heat. It is typically expressed as

$$RR = \frac{\left| \dot{Q}_{\text{fwd}} \right| - \left| \dot{Q}_{\text{rev}} \right|}{\left| \dot{Q}_{\text{rev}} \right|} \quad (1)$$

where $\dot{Q}_{\text{fwd}}$ and $\dot{Q}_{\text{rev}}$ are the heat fluxes in the forward and reverse direction when $|\dot{Q}_{\text{fwd}}| > |\dot{Q}_{\text{rev}}|$.

ii. *Thermal bias*: It is the difference of temperature across the device, where T_{h} and T_{c} correspond to the temperatures of the heat source (hot terminal) and the heat sink (cold terminal).

2.1. Two-Segment Thermal Diodes

The simplest design of a thermal diode in solid state is based on two-segment materials. Such a device consists of a combination of two different material blocks with dissimilar thermal properties.[1] The basic idea to achieve thermal rectification is that the two materials have a different thermal conductivity dependence with temperature.[35–38] Under this condition, an inversion of the thermal bias (temperature gradient) direction will result in a different magnitude of the heat flow (forward vs reverse) due to a change in the effective or overall thermal conduction across the two-segment material structure.[1]

In Section 2.1, we differentiate between three approaches to develop a thermal diode based on two-segment materials. First, we explain devices in which the two material blocks have opposite thermal conductivity trends with rising temperature. For the sake of convenience, we define them as junction of materials with different thermal properties (JMT) diodes. Afterward, we explain phase change material (PCM) diodes. In these diodes, a solid-to-solid phase change is the basis for thermal rectification. Then, we explain thermal diodes based
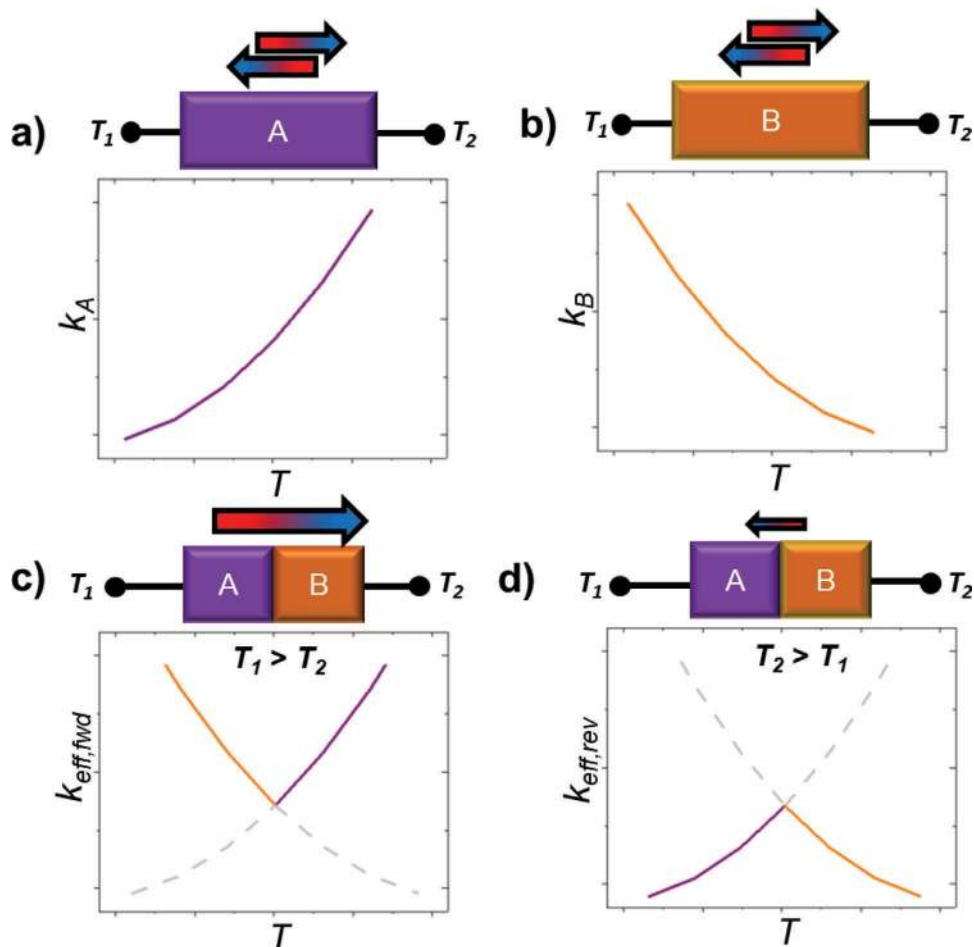
**ADVANCED
SCIENCE NEWS**
www.advancedsciencenews.com

**ADVANCED
ELECTRONIC
MATERIALS**
www.advelectronicmat.de

Figure 2. Schematic drawing of the thermal conductivity (k) as a function of the temperature (T) in a JMT diode. a,b) Thermal conductivity of block A and of block B separately. c,d) Effective thermal conductivity (k_{eff}) (continuous line) of the JMT diode in the forward and reverse direction.

on radiative heat transfer. Finally, we present theoretical approaches for the design of high rectification two-segment thermal diodes.

2.1.1. Junction of Materials with Different Thermal Properties (JMT)

A JMT thermal diode is a two-segment material thermal diode made of two dissimilar material blocks, e.g., block A and block B.[36,37] These two blocks present different temperature (T) dependent thermal conductivity (k) trends, as presented in **Figure 2**. Figure 2a,b illustrates the thermal conductivity of the two material blocks k_A and k_B as a function of the temperature. Figure 2a shows that material block A has an increase in the thermal conductivity with increasing temperature. Figure 2b shows that the thermal conductivity of material block B is decreasing with increasing temperature. To understand how such a material system leads to thermal rectification, we must consider the effective thermal properties of the two-segment material structure depending on the thermal bias directionality. Hence, we need to consider two cases, i.e., when the thermal

bias is applied in the forward (A → B) versus the reverse direction (B → A).

Figure 2c,d illustrates the effective thermal conductivity of the material junction A-B structure in the forward and reverse direction. In the forward direction, a temperature gradient from the hot block A to the cold block B is established. Therefore, the effective thermal conductivity ($k_{eff,fwd}$) of the segment structure, i.e., continuous purple (block A) and orange lines (block B) of Figure 2c), is high in the forward direction. In the reverse configuration, the temperature gradient is established from the hot block B to the cold block A. In this case, the thermal conductivity trend of both blocks is now reversed compared to the forward case. As a result, the effective total thermal conductivity ($k_{eff,rev}$) of the two-segment structure is lower than in the forward direction, i.e., continuous purple (block A) and orange (block B) lines of Figure 2d. Hence, the total heat flux is expected to be higher in the forward direction in comparison to the reverse configuration under the condition that the temperatures of the terminals (T_h and T_c) are held constant.

Figure 3 shows the thermal conductivity trends of some materials as a function of temperature.[1,39–44] These are in agreement with the theory of thermal transport expected for
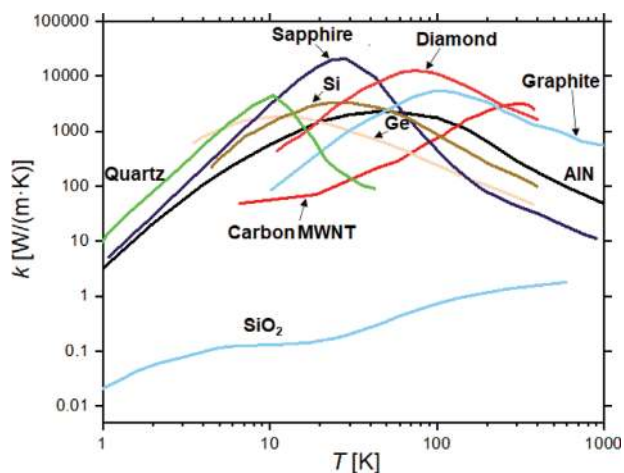
Figure 3. Thermal conductivity (k) of some materials as a function of the temperature (T). Data from refs. [1,39–44].

these materials.[45–47] From a simplistic point of view, the temperature-dependent thermal conductivity ($k(T)$) trends of typical materials can be described as: i) At low temperatures, $k(T)$ is increasing with T due to the increase of the heat capacity until it reaches a peak.[45,48] The peak position and magnitude of the thermal conductivity depends on the material. ii) At higher temperatures, the thermal conductivity decreases due to a reduction in the phonon mean free path (MFP).[45,48] A combination of two materials with thermal conductivity peaks at different temperatures will result in the desired two-segment material junction structure.

In general, the thermal conductivity peak is reached below room temperature for most of the materials presented in Figure 3. Additionally, there are some materials that present an increase of the thermal conductivity at room temperature (e.g., carbon nanotubes,[40] amorphous silicon oxide,[39] or caloric materials like gadolinium[49]). To take advantage of the asymmetry in the effective thermal properties of the two blocks that form part of the JMT diode, the design is usually limited to low temperatures. Jeżowski and Rafalowicz[33] developed the first JMT diode experimentally in 1978. The authors investigated a junction of graphite and quartz considering absolute temperatures between 6 and 95 K. The peak of the thermal conductivity of quartz can be found near 6 K.[44,50] In graphite this peak in the thermal conductivity is reached at around 100 K, as can be seen in Figure 3.[43,51] On the one hand, for temperatures below 100 K, graphite presented an increase in the thermal conductivity with rising temperature (block A). On the other hand, the thermal conductivity of quartz decreased for temperatures above 6 K (block B). This thermal diode reached a maximum rectification of RR = 70% for a thermal bias of 40 K between heat source and heat sink.[33] Similarly, Kobayashi et al.[35,52] investigated LaCoO$_3$/La$_{0.7}$Sr$_{0.3}$CoO$_3$ (LCO/LSCO) structures for thermal rectification. LSCO had an increasing $k(T)$ with rising temperature, while LCO presented a decreasing $k(T)$ behavior below 200 K. The authors observed a thermal rectification of RR = 43% between 40 K (heat sink) and 98.9 K (heat source).[35]

2.1.2. PCM Thermal Diodes

A PCM thermal diode is another type of two-segment material thermal diode. Here, the two-segment structure is made of a PCM block and a phase invariant material (PIM) block. On one hand, a solid-to-solid structural change of the PCM occurs at a critical transition temperature, T_{crit}, leading to a variation of the PCM thermal conductivity. On the other hand, the phase of the PIM remains invariant at the temperature of application. Bringing together a PCM and a PIM can lead to thermal rectification by taking advantage of the thermal conductivity change due to the phase transition of the PCM block. When the PCM block is in direct contact with the heat source and the temperature is higher than the transition temperature, a phase change in the PCM material is induced. However, in the reverse case, when the temperatures in the PCM block are lower than the transition one, no phase change occurs. Therefore, two different effective thermal conductivities result from applying a gradient of temperature in the forward versus reverse direction. Recently, some scientific publications showed that a combination of two different PCMs is a promising approach to achieve high thermal rectification which may exceed values obtained by the regular PCM/PIM structures.[53–55]

In many PCMs, the change in the thermal properties occur in a small temperature range (few K) due to a change in the material crystalline structure when the temperature is higher than T_{crit}.[56–58] For that reason, in comparison to JMT diodes, high rectification ratios can already be achieved for small thermal biases (few K).[56] However, the main challenge of PCM diodes is to choose a material that exhibits a phase change resulting in a large difference in thermal conductivity. As an example, vanadium dioxide (VO$_2$) is a PCM that has been used for thermal diodes.[59,60] VO$_2$ presents a metal insulator phase transition (MIT) near room temperature.[61] **Figure 4** depicts the MIT in VO$_2$ and its change in the thermal conductivity. Figure 4a shows that VO$_2$ has a monoclinic insulating state that typically changes to a rutile tetragonal metallic state when the temperature rises above $\approx$340 K. The thermal conductivity increases across this phase transition.[57,58] As an example, Oh et al.[57] reported $\approx$60% increase of k (from $k \approx 3.5$ W m^{-1} K^{-1} to $k \approx 5.5$ W m^{-1} K^{-1}) in thin film VO$_2$ as a consequence of the phase change. The reason for this thermal transition is based on the changes in the band structure and the influence of the electronic heat transport, illustrated in Figure 4b.[57,62] While in the insulating state the valence band d$_{ll}$ is separated from the conduction band due to a large bandgap, the two bands overlap in the metallic state.[62] As a result, the electrical conduction is increased and hence the thermal conductivity, given the influence of the electrons as heat carriers. It is also worth noting that VO$_2$, like other PCMs, might present hysteresis, meaning that the temperature at which the phase change happens when cooling versus heating might shift slightly.[63]

An example of a PCM diode using VO$_2$ is illustrated in **Figure 5**. This structure corresponds to the thermal diode based on a VO$_2$/sapphire material combination which is reported by Ordonez-Miranda et al.[70] In the forward direction, the heat is flowing from the VO$_2$ heat source to the sapphire heat sink. The temperature at the heat source is above T_{crit} = 340 K, inducing VO$_2$ block to transition to its metallic state. However, in the reverse direction,
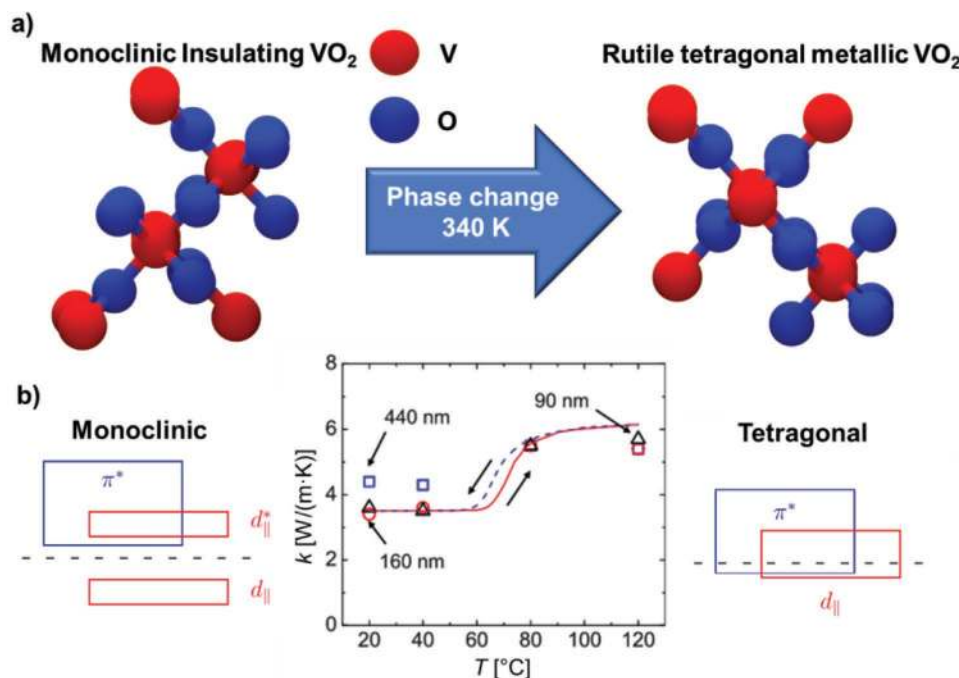
Figure 4. Schematic drawing of the changes of VO$_2$ at its phase transition. a) Crystallographic structure phase change at 340 K from a monoclinic to a tetragonal phase, b) Simple band diagrams and plot of the thermal conductivity (k) changes along the phase transition of VO$_2$ films with thicknesses ranging from 90 to 440 nm as a function of the temperature (T), based on the work of Oh et al.[57] and Eyert.[62] Thermal conductivity vs. temperature graph in (b) adapted with permission.[57] Copyright 2010, AIP. Band diagrams adapted with permission.[62] Copyright 2002, Wiley-VCH Verlag. Data for the crystal structures in (a) from refs. [64–69].

the VO$_2$ block is now at the insulating phase because the temperature is below its transition temperature. The phase of sapphire remains the same in both scenarios, i.e., PIM block. Under this scenario, the effective thermal conductivity of the PCM diode in the forward direction is higher than in the reverse one.

Kobayashi et al.[56] developed a millimeter-sized PCM thermal rectifier based on La$_{1.98}$Nd$_{0.02}$CuO$_4$ (PIM) and MnV$_2$O$_4$ (PCM). MnV$_2$O$_4$ has a structural phase change at T_{crit} = 57 K that leads to an abrupt decrease in the thermal conductivity as the temperature increases. At this temperature the structure is converted from a tetragonal phase with a high thermal conductivity to a cubic phase with a lower one.[56,71] The authors observed a thermal rectification of RR = 14% for a temperature span between 55.4 K (heat sink) and 57.4 K (heat source), which can be considered as a high value considering the small thermal bias below 2 K.[56] Additionally, Garcia-Garcia and Alvarez-Quintana[72] investigated the thermal rectification in a nitinol/graphite PCM thermal diode. In this case, nitinol was used as the PCM and graphite as the PIM. Nitinol has a structural phase change at around T_{crit} = 330 K from a monoclinic martensite phase to a cubic austenite phase at temperatures higher than the transition one.[72] The authors observed a rise in the thermal conductivity of the nitinol from k ≈ 7.8 W m^{-1} K^{-1} in the martensite to k ≈ 17.3 W m^{-1} K^{-1} in the austenite phase. The authors observed a maximum thermal rectification of RR = 47% obtained at a temperature of 290 K with a thermal bias of 160 K.[72] The thermal conductivity rose gradually above the phase transition temperature and not stepwise, which

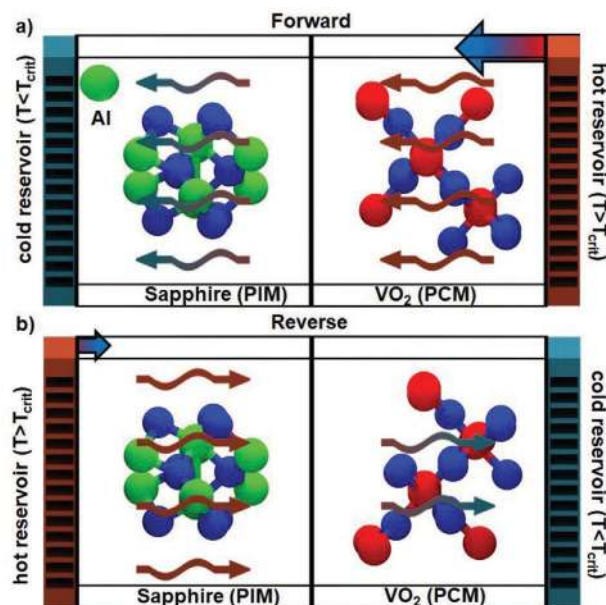resulted in a significant enhancement of the thermal rectification at higher temperatures.

Figure 5. Schematic drawing of a sapphire/VO$_2$ diode. a) Heat flux in forward direction (from the hot VO$_2$ to the cold sapphire), and b) heat flux in reverse direction (from the hot sapphire to the cold VO$_2$). The arrows show the direction of heat and indicate that the higher heat flux is in the forward direction. Data from refs. [64–69].

2000625 (5 of 28)

**ADVANCED
SCIENCE NEWS**
www.advancedsciencenews.com

**ADVANCED
ELECTRONIC
MATERIALS**
www.advelectronicmat.de

2.1.3. Thermal Radiative PCM Diodes

Among thermal diodes that use phase change materials, we must distinguish between classical PCM diodes, explained in Section 2.1.2, and thermal radiative PCM diodes. The design of radiative PCM devices is similar to the standard combination of a PIM and a PCM material block but with a gap (vacuum) between them. In these thermal diodes, the heat is transferred by radiation between the two material blocks.

Radiative PCM thermal diodes are typically designed in two separate regimes. These are defined as far-field and near-field regimes, presenting a relatively large (above 10 µm) and small (well below 10 µm)[59,73] gap between blocks. In the far-field regime, the radiative heat transport is mainly based on the fundamental heat transport theorems of Stefan–Boltzmann and Planck.[73,74] In the near-field regime, an enhancement of the radiative heat transport beyond the blackbody limit has been observed.[73,75] Shen et al.[75] investigated the radiative heat transport between two gold plates paying special attention to the distance between them. The authors observed a strong increase in the heat transport for gaps below 100 nm. The authors claimed that the likelihood that nonresonant surface waves can tunnel through the gap increases for smaller distances. These nonresonant surface waves participated in the heat transport; hence, a higher heat flux was observed in the near-field than in the far-field regime.

As an example, Ito et al.[60] presented a far-field thermal diode with fused quartz as the PIM and VO_2 as the PCM with a vacuum gap of 1 mm between them. The heat transport between the material blocks occurred via mid-infrared radiation. In the insulating state of VO_2, the absorbance for the mid-infrared thermal radiation was enhanced. However, in the metallic state the reflectance of mid-infrared radiation was increased. In contrast to the VO_2–sapphire diode illustrated in Figure 5, the preferred direction of the heat flux was from the heat source PIM to the heat sink insulating VO_2. The authors observed a maximum rectification ratio of RR ≈ 180% at a temperature span between 300 K (heat sink) and 360 K (heat source). Additionally, the authors succeeded in reducing the phase transition temperature of VO_2 from $T_{crit} = 340$ K to $T_{crit} = 315$ K by doping it with tungsten (1 at%). As a result, such diodes can be used at almost room temperature, without any major reduction in the rectification ratio.

Fiorino et al.[59] worked on a microsized thermal diode that works in the near field with a similar material configuration as indicated in Figure 5, i.e., VO_2 as PCM and in this case Si as PIM block. In this specific device, the vacuum gap was varied from above 1000 nm down to 140 nm. The authors observed a maximum thermal rectification above RR ≈ 50% for the smallest gap (140 nm) at a temperature span between 294 K (heat sink) and 364 K (heat source). Under this scenario, the heat flux was larger as the temperature gradient was set from the hot metallic PCM phase (VO_2, heat source) to the cold PIM block (doped Si, heat sink). The authors computed their diode structure using a fluctuational electrodynamics based approach to verify their experimental results. The theoretical results confirmed the higher heat flux in the forward direction. The authors claimed that the free electrons in the metallic VO_2 and in the doped Si strongly absorbed photons with a frequency below 10^{14} rad s^{-1} in the forward direction. In the reverse direction, the propagation of surface phonons was suppressed due to the poor coupling of the phonon modes in the isolating VO_2 and the Si. As a result, the authors stated that the heat flux was strongly enhanced in the forward direction, while being lower in the reversed case.

2.1.4. Theoretical Predictions of PCM Diodes

In addition to the experimental thermal diodes presented above, several thermal PCM diodes have been reported theoretically. In this section, we present theoretical approaches that obtained high rectification values using new materials and geometries.

Ghanekar et al.[24] simulated the heat transport in a VO_2–boron nitride (BN) diode based on near-field radiation heat transport. In this model, VO_2 was working as the PCM and BN as the PIM. While the concept was similar to the thermal diode in Section 2.1.3,[59] the VO_2 was designed in a grating form with several VO_2 blocks containing a small gap between each other (≈50 nm). A maximum thermal rectification of RR ≈ 1400% was calculated between 331 K (heat sink) and 351 K (heat source) for a gap between the PCM and PIM block ≈100 nm, a height/width of the VO_2 blocks of ≈500/150 nm. The authors compared the calculation to a nongrating VO_2 structure, showing a much lower RR < 100% than with the grating diode.[24] The near-field radiative heat transfer between the two blocks was theoretically obtained by using a Green's function formalism in both cases.[24] The authors claimed that in the grating structure, the phonon tunneling was strongly reduced in the reverse direction leading to an extremely low heat flux, while the heat flux in the forward direction almost stayed unchanged.[24] Hence, an extremely high thermal rectification was obtained in this particular design.

Zhang and Luo[76] used molecular dynamics (MD) to determine the potential of some types of polymers for the design of a PCM thermal diode. The authors simulated the thermal rectification behavior in a polyethylene nanofiber (PE)/crosslinked PE (PEX) two-segment system. PE has a structural phase change slightly above room temperature (the exact value depends on the fiber diameter) going from an ordered crystalline structure to a disordered structure. This results in a drastic reduction of the thermal conductivity. Since the PEX is phase invariant, the effective thermal conductivity varied due to the changes in the PE phase. This PE-PEX diode structure was simulated for different fiber diameters, achieving a thermal rectification near room temperature of RR ≈ 74% when applying a temperature gradient between 312 K (heat sink) and 332 K (heat source).

Joulain et al.[77] theoretically investigated the thermal rectification in a SiC/SiO_2 radiative thermal diode based on near-field thermal radiation by using a fluctuational electrodynamics formalism. The temperature was set from 297 K (heat sink) to 1470 K (heat source). For the base of their calculations, the authors used measured optical data of both materials at the evaluated temperatures. The authors claimed that the spectral heat flux was strongly reduced in the hot SiC, and mildly reduced in SiO_2. As a result, the authors observed a higher heat flux when the SiC was in contact to the heat sink. The authors obtained a maximum rectification ratio of RR ≈ 250% for a gap

ADVANCED
SCIENCE NEWS
www.advancedsciencenews.com

ADVANCED
ELECTRONIC
MATERIALS
www.advelectronicmat.de

below 10 nm. Basically, this diode can be seen as a combination of the thermal radiative diode presented in Section 2.1.3 and the JMT diode presented in Section 2.1.1, as the two materials have dissimilar (in this case optical) properties. A similar case was obtained by Wang and Zhang[78] in a near-field intrinsic Si/doped Si thermal radiative diode. The authors theoretically analyzed the heat flux when the temperature was set between 300 K (heat sink) and 1000 K (heat source). Similarly, as the project presented before, the authors used fluctuational electrodynamics to calculate the differences in the heat flux in both directions. In the forward direction, when the heat source was in contact to the intrinsic Si, heat carriers got thermally excited. In this case, the free carrier concentration of the intrinsic Si was close to the free carrier concentration of the doped Si, enabling a high heat exchange between the blocks. As a result, a high near-field heat flux was expected. In the reverse direction when the heat sink was in contact with the intrinsic Si, the carriers concentration remained low and it acted as a nonabsorbing medium, leading to a lower heat flux. The authors calculated a lower heat flux in the reverse case with a maximum rectification of RR ≈ 6700% with a hypothetical gap at sub-10 nm between the two blocks.

Martinez-Flores et al.[79] theoretically investigated a two-segment diode based on two different $La_{1-x}Sr_xMnO_3$ ferromagnetic manganites by means of Fourier's law. In ferromagnetic materials, the heat is additionally transported due to magnons, which is explained more in detail in Section 3.2. The thermal conductance changed drastically when the material is beyond the Curie temperature. By varying the composition of the material, the transition temperature was varied and thus a material diode with two different transition temperatures was designed. The authors calculated a maximum thermal rectification of above RR ≈ 70% by using a $La_{0.7}Sr_{0.3}MnO_3/La_{0.82}Sr_{0.18}MnO_3$ material combination.[79]

Additionally, Roberts and Walker[80] stated that the poor quality of interfaces can lead to a reduction of the thermal rectification. Thus, it can happen that a material system which

theoretically should rectify heat shows no visible thermal rectification due to scatter process at an imperfect interface.

2.2. Material Engineering

In the previous section, we explained two-segment thermal diodes based on materials with varying or different thermal properties. However, thermal rectification can also be achieved by material engineering.[26,29] A measure that indicates how well heat is transported by electrons and phonons is the MFP, among others.[45] Material engineering could be used to modify the MFP of these heat carriers by varying scattering events through the modification of the shape,[81,82] size,[83–86] and/or the physical/chemical properties (grain boundaries,[87–89] impurities,[90–92] etc.) of the material.[93] Given the average MFP of most of the materials, this method of engineering has a major influence at the micro and nanoscale.[93,94] Additionally, the absolute temperature of the material also affects the scattering rate of the phonons, leading to a change of the thermal conductivity.[48]

This section summarizes thermal diodes in the micro and nanoscale that use material engineering to customize the heat carrier transport depending on directionality. First, we present shape-induced thermal diode (SID) systems where an asymmetrical shape of the material induces thermal rectification. Second, we explain defect-induced thermal diodes (DID), in which an asymmetrical modification of the structure leads to thermal rectification.

2.2.1. Shape-Induced Thermal Diodes (SID)

A SID is a material structure with an asymmetric shape. **Figure 6** illustrates some examples of asymmetric structures that have been investigated for thermal rectification.[95–99] Most of the research carried out in this field was based on graphene
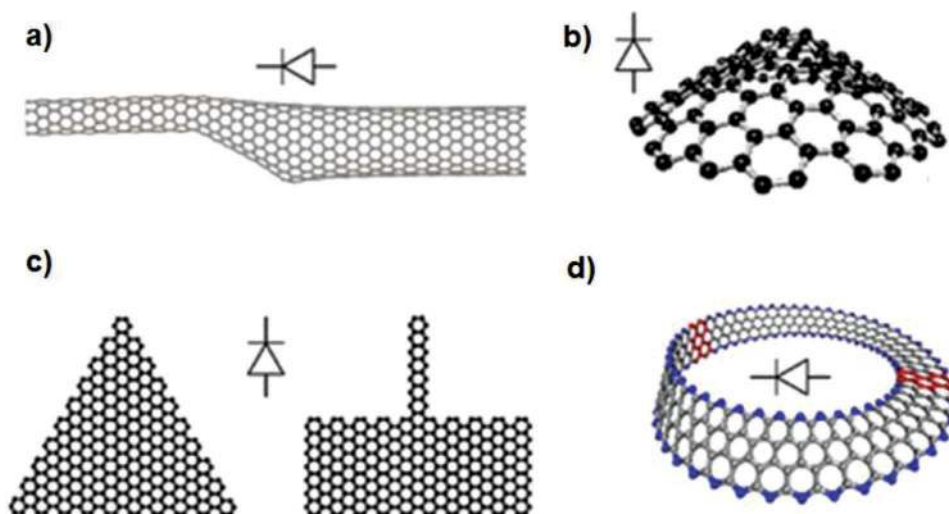

Figure 6. Schematic drawings of different graphene thermal diodes with asymmetric shape and the indicated preferred direction of the heat flux: a) nanotube beam, b) nanocone structure, c) asymmetric nanoribbons, and d) Moebius graphene stripe. Reproduced with permission.[95] Copyright 2012, American Physical Society.
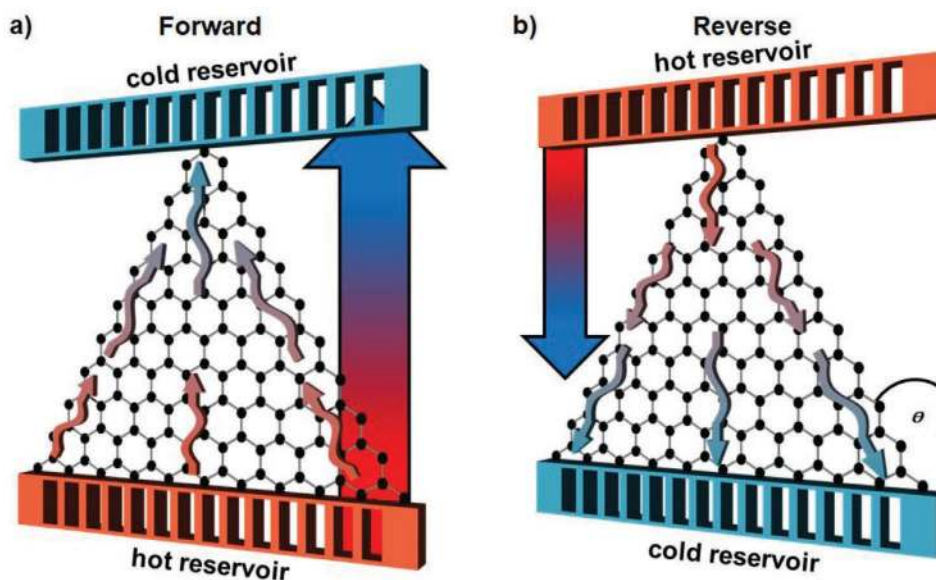
ADVANCED
SCIENCE NEWS
www.advancedsciencenews.com

ADVANCED
ELECTRONIC
MATERIALS
www.advelectronicmat.de

Figure 7. Schematic drawing of shape-induced thermal rectification in a triangular graphene ribbon; a) Heat flux in forward direction from the wide side to the narrow side, and b) reduced heat flux in reverse direction due to bottleneck effect in the narrow side with its representative opening angle Θ.

structures. The long MFP of phonons in graphene near room temperature[100,101] facilitates the tuning of the thermal properties via material engineering without the need of developing structures with extremely small size.

As an example, asymmetric structures typically have a wide side versus a narrow one (e.g., nanoribbon structures in Figure 6c). The wider side is typically in the order or larger than the average MFP of the phonons. However, the narrower side is below it, causing an increment of phonon scattering due to size confinement effects.[34,102] Considering a triangular asymmetric graphene sample as a case of study, we now analyze the following two scenarios for thermal rectification: i) forward direction, when the wide graphene side is at the heat source and the narrow side is at the heat sink; ii) reverse direction, when the gradient of temperature is inverted. In the reverse direction, the phonon density is high at the narrower end due to the high temperature. Besides the regular scattering processes, the scattering off boundaries becomes significant. This leads to a drastic decrease in the MFP of phonons at the hot narrow graphene side area. The phonons seem to be partially trapped in this region, which is described as bottleneck.[34] However, in the forward direction the temperature at the narrow end is significantly lower resulting in a smaller impact of boundary scattering. **Figure 7** illustrates this effect. The phonons can propagate better in the forward direction than in the reverse direction, where they seem to be trapped at the narrow side. As a result, the heat flux is diminished in the reverse direction. Wang et al.[34] investigated thermal rectification in a triangular graphene structure similar to the one shown in Figure 7. The authors observed a maximum thermal rectification of about RR ≈ 11% for ≈5 and ≈2 µm at the wide and narrow side, respectively.

Further investigated structures are presented in **Figure 8**. Chang et al.[28] were pioneers in developing asymmetric thermal diodes. For that purpose, the authors used boron nitride nanotubes (BNNT) and carbon nanotubes (CNT) where

one end is mass loaded with trimethyl-cyclopentadienyl platinum ($C_9H_{16}Pt$), as illustrated in Figure 8a. As a result, the mass loaded side could be seen as the wider side that presented more channels for the heat to flow than the narrower one. Following the theoretical predictions of shape-induced nanosized structures, the heat flux was higher along the decreasing width, i.e., the high to the low mass side.[98] This was experimentally confirmed, obtaining a thermal rectification of RR ≈ 7% at room temperature.

Additionally, Zhu et al.[103] proposed a thermal rectifier based on a VO_2 beam with a tapered width. Figure 8b shows a scanning electron microscopy (SEM) image of this diode. This device was developed at the microscale and its thermal properties were investigated considering a low thermal bias below 1 K.[103] The heat flow was enhanced from the hot wide side to the cold narrow side. The authors observed a maximum rectification of RR ≈ 28% at an absolute temperature around 300–320 K.[103] Additionally, the authors claimed that the transition temperature of VO_2 beam and the diode performance could be engineered by doping it with tungsten or by applying local stress.[103]

Tian et al.[104] evaluated the thermal rectification in a junction of two rectangular shaped graphene oxides with different sizes at room temperature. In this junction, the average temperature of the diode was lower when the temperature gradient was applied from the small rectangle to the big one. Due to the decreasing $k(T)$ trend of graphene oxide at room temperature, the effective thermal conductivity was higher in this case. As a result, a maximum thermal rectification of RR ≈ 9% was observed experimentally, which was confirmed by classical heat transport finite element modeling (FEM).[104] Therefore, temperature in the structure was set to 300 K (heat sink) and 347 K (heat source) in the experiment as in the model.[104] The thermal conductivity properties of graphene oxides can be further tuned by applying pressure.[105] Similarly, Sawaki et al.[52] investigated the thermal rectification in an asymmetric pyramid shape of
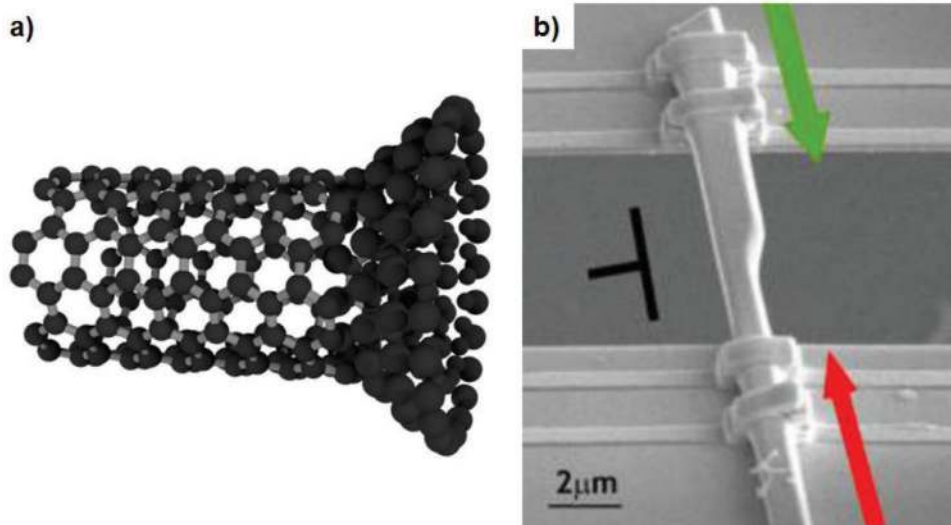
**ADVANCED
SCIENCE NEWS**
www.advancedsciencenews.com

**ADVANCED
ELECTRONIC
MATERIALS**
www.advelectronicmat.de

Figure 8. a) Schematic drawing of the mass loaded nanotube thermal rectifier similar to the one presented by Chang et al.[28] b) SEM image of an asymmetrical VO_2 beam investigated by Zhu et al.[103] The arrows indicate the heat fluxes in the two directions showing a larger flow from the wide to the narrow side of the beam. b) Reproduced with permission.[103] Copyright 2014, American Chemical Society.

the LCO/LSCO diode (from a wider LCO to a narrower LSCO) mentioned in Section 2.1.1. For these structures, the authors observed a thermal rectification of RR ≈ 35%. The authors used Fourier's law to analyze the experimental results.[52] In these cases, we need to consider that the size of the investigated devices was at the size of few mm.

Muñoz Rojo et al.[106] investigated the potential thermal rectification properties of step graphene junctions, defined as steps between regions with different number of graphene layers. The heat flow across graphene junctions from monolayer to bilayer graphene, as well as bilayer to four-layer graphene, were measured for the first time in both directions (forward vs reverse). While these graphene junctions were previously theoretically predicted to present high thermal rectification ratios (RR up to 100% and higher),[107] the decoupling between layers controlled the thermal transport showing no evidence of thermal asymmetry. To verify their results nonequilibrium molecular dynamic (NEMD) simulations were performed.[106]

2.2.2. Theoretical Predictions of SIDs

In addition to the experimental thermal diodes presented above, several theoretical SID structures have been reported. Yang et al.[108–110] used NEMD simulations to predict ultra-high thermal rectification in junctions with single-wall carbon nanotubes (SWCNT) and graphene (PGNs). In this diode, a SWCNT with a narrow area was connected to a 2D graphene sheet with a wide area. In a more advanced version, an additional graphene sheet with a smaller area was also added. The graphene layers were connected to each other with SWCNT pillars as connecting channels. In both structures, the authors obtained thermal rectification ratios from RR ≈ 800% up to RR ≈ 1600%, with a maximum at a temperature between 100 K (heat sink) and 300 K (heat source). Similar to prior experiments, the heat flux was strongly inhibited when it flowed

from the narrow side (free end of the carbon nanotube) to the wide side (ground graphene sheet). The main reason for thermal rectification was related to the large mismatch of the density of states of heat carriers between the wide and the narrow side in reverse direction.[108–110] For a detailed description of the physical mechanisms, the authors referenced previous theoretical work conducted by Lee et al.[111] In this publication, the authors investigated thermal rectification in a pyramid-shaped diamond nanostructure in a NEMD simulation. The authors claimed that the number of atoms at the narrower side was small, hence collective vibrations were induced. At the wider side, this effect was negligible due to the much larger contact area. The collective vibrations were temperature dependent, resulting in a large mismatch in the density of states between the wide and narrow side in reverse direction leading to a lower heat flux.[111] The same principle can be applied to the simulation results of Yang et al.[108–110] In another publication, Yang et al.[112] investigated a similar structure, but consisting of a junction of double-layered graphene and double-walled carbon nanotubes (DGN-DWCNT). In this case, the authors obtained a maximum thermal rectification of above RR ≈ 1200% with 100 K (heat sink) and 300 K (heat source) along the structure.

Ma and Tian[113] performed a NEMD simulation presenting a thermal diode based on a tapered PS-PNb polymer with an asymmetric shape. Their design consisted of polystyrene (PS) chains connected perpendicularly to the polynorbornene (Pnb) backbone and with a chain length that decreased along the diode structure. The authors stated that in forward direction (wide to narrow end) the heat was flowing diffusively between the side chains, whereby in the backward direction (narrow to wide end) the heat flowed ballistically along the backbone. As opposed to other SID diodes, the heat flux was higher from the narrow to the wider end. The results showed a maximum thermal rectification of RR ≈ 70% at a temperature span between 100 K (heat sink) and 300 K (heat source).
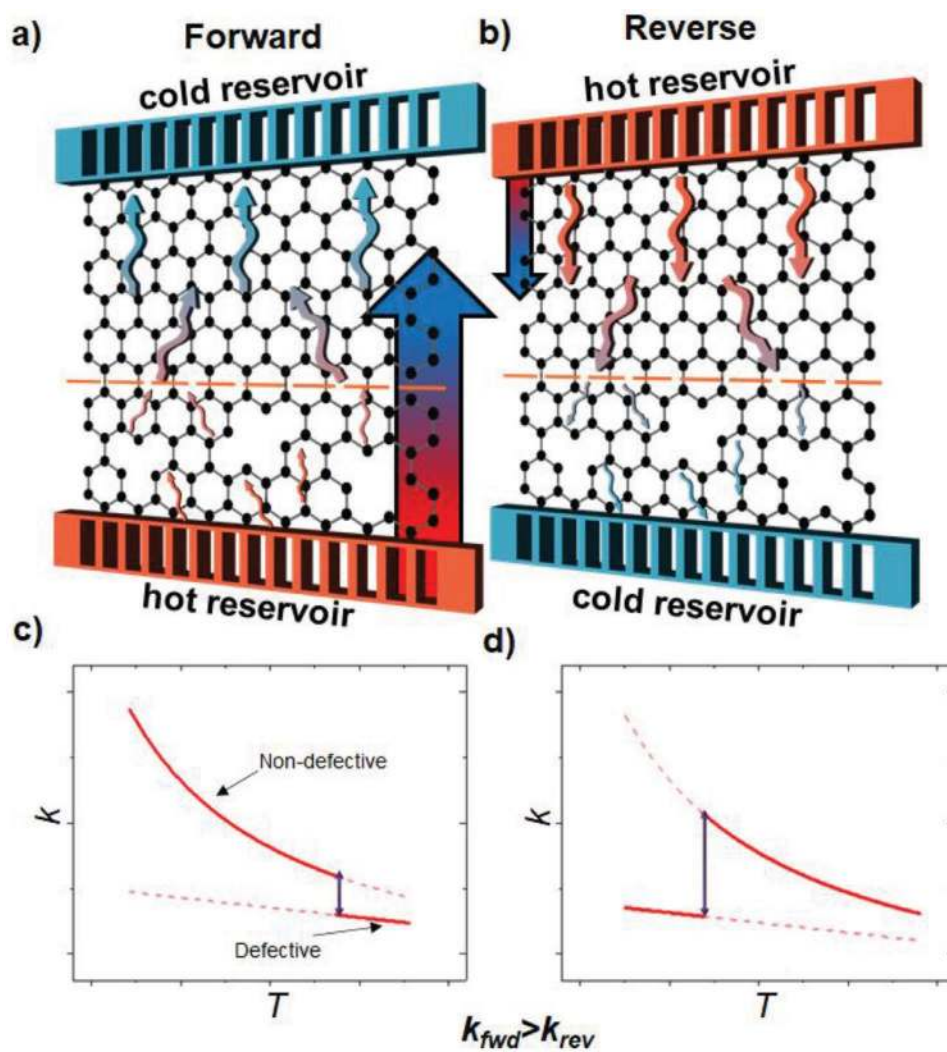
Figure 9. Schematic drawing of thermal rectification in a partially defective graphene structure: a,b) The heat fluxes across the structure in the forward and reverse direction, respectively. c,d) Schematic drawing of the thermal conductivity (k) of the two cases above as a function of temperature (T). The solid lines show the effective thermal conductivity along the temperature gradient.

Carlomagno et al.[114] carried out a mathematical analysis based on Fourier's law on the thermal rectification in Si_xGe_{1-x} ($0 \leq x \leq 1$) alloy nanowires. In their model, the authors used an either pure Si or Ge core with a gradual composition to a Ge or Si shell, respectively, to evaluate whether there was heat flow asymmetry from the core to the shell versus the shell to the core. The authors obtained a higher heat flux from a Si shell toward a Ge core with a maximum rectification value of RR ≈ 170%.[114]

2.2.3. Defect-Induced Thermal Diodes (DID)

A DID is developed by inducing an asymmetric set of defects, impurities, or other types of structure modifications in the material. Examples of such types of structural modifications are the deposition of stranger atoms or milling of nanosized holes in the material.[34] In order to explain how thermal rectification occurs in defect-induced diodes, we take as a case of example

the graphene diode developed by Wang et al.[34] This thermal diode consists of a junction of two different graphene regions, one with defects and another one nondefective. The defective region at one side of the graphene is generated by nanoporous milling via focused ion beam (FIB). **Figure 9** illustrates the heat flow in the forward and reverse direction as well as a simplified view of the phonon propagation inspired by the work of Wang et al.[34]

In the forward direction indicated in Figure 9a, the heat source is in contact to the defective graphene. At the heat sink, the phonon density and the Umklapp scattering are low, which result in a high MFP of the phonons. From the heat sink to the heat source, the phonon density in the material increases. The scattering of the phonons with the impurities is the major scattering mechanism in the defected region, which is defined by the pore size and its density. The temperature dependence of the thermal conductivity (k) of each region, defective versus nondefective graphene in the forward direction, is represented in Figure 9c. The solid red line indicates the thermal

conductivity trend for each region under the forward direction configuration.

In the reverse direction, indicated in Figure 9b, the heat source is connected to the nondefected graphene side. At the heat sink, the phonon density is low in the defective region. However, as already explained before, the dominant scattering process in this region is the phonon impurity scattering. On the one hand, the MFP in the defective region slightly differs with temperature and strongly depends on the pore density and size. On the other hand, in the nondefective region the thermal conductivity is increasing when going from the hot side to the junction due to the decreasing phonon density. The solid red lines of Figure 9d indicate the thermal conductivity (k) trend for each region under the reverse direction configuration. While in the forward direction a small mismatch between the thermal properties at the defective/nondefective interface occurs, this effect is bigger in the reverse case. The mismatch in thermal properties leads to different effective thermal conductivities depending on the directionality of the heat flux ($k_{fwd} > k_{rev}$), resulting in thermal rectification.[34]

Wang et al.[34] investigated three different samples, with a similar structure as the one explained above with different pore densities and sizes in a high vacuum chamber. The authors fabricated graphene sheets with the dimensions of few micrometers. A maximum rectification of RR ≈ 28% was observed under the following configuration: 14 nanopores with a diameter of 100 nm. These results agreed well with a previous theoretical work done by Takahashi et al.[115] In this work, the authors predicted that the heat flow in a half vacancy defected single-wall carbon nanotube is enhanced in the direction from the defective to the pristine region.

Additionally, Wang et al.[34] deposited carbon nanoparticles by electron beam on one side of a similar graphene nanosheet. The carbon deposited region of the graphene acted as a bottleneck for phonons similar to the one explained in Section 2.2.1.
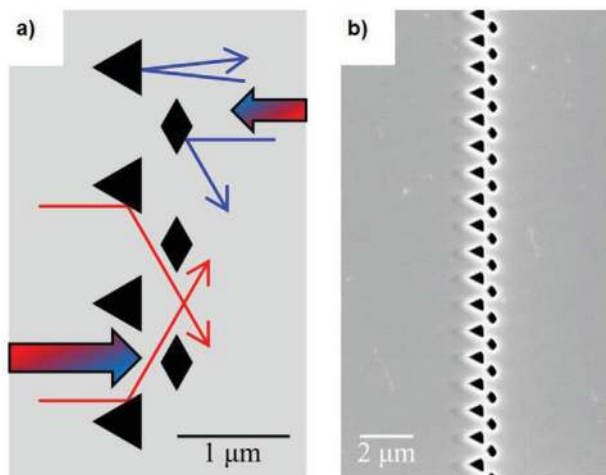

Figure 10. Thermal rectification in a milled silicon membrane investigated by Schmotz et al.[116] a) Schematic drawing of a milled silicon membrane with triangular and rhombic holes. This structure results in a variation of the heat flux depending on the directionality, as indicated by the arrows. b) SEM images of the thermal diode. Reproduced with permission.[116] Copyright 2011, IOP Publishing and Deutsche Physikalische Gesellschaft.

The authors obtained a maximum thermal rectification of about RR ≈ 10%.[34]

Other materials beyond graphene have been used to develop thermal diodes. Schmotz et al.[116] proposed a thermal diode based on a silicon membrane as presented in **Figure 10**. An array of triangular and rhombic holes was milled with FIB on the membrane. Figure 10a illustrates this type of structure that results in different scattering mechanisms depending on the heat flow direction. On the one hand, the forward direction is indicated by the single red arrows. The array of holes is designed to facilitate the flow of reflected phonons at the triangular holes. On the other hand, the reverse direction is indicated by the blue arrows. In this situation, the phonons backscatter at the backside of the array, which leads to a reduction of the thermal transport in this direction. This type of diode mostly worked at low temperatures, around ≈150 K, in which phonon–phonon scattering is not dominant. Figure 10b shows an SEM image of the array of holes. A laser was used to heat up (temperature rise of ≈70 K) the surface at both sides of the array to account for thermal rectification. The maximum rectification ratio observed for this diode was RR ≈ 70%.

2.2.4. Theoretical Predictions of DIDs

The use of defects to create thermal rectification was investigated theoretically in different ways. In the following section, we present approaches based on the implementation of vacancies, foreign atoms, or grain boundaries in materials to obtain thermal rectification.

Guo et al.[117] proposed a defect-induced thermal diode based on N-doped graphene by means of a reverse NEMD simulation at different temperatures (200, 300, and 600 K). A defect with a triangular asymmetric shape was designed in the center of a graphene layer. Similar to the blocking array of Schmotz et al.[116] the phonon scattering was bound to be higher at the wider side of the triangle, which showed a reduction of the heat flux against this side. Then, the simulation was repeated under the scenario where the triangular defect is surrounded by nitrogen (N) doping atoms. In the undoped case, a rectification of RR ≈ 10% was obtained at an average temperature of 600 K. However, by varying the concentration of nitrogen doping the rectification increased up to a maximum of RR ≈ 24%. In a similar NEMD approach, Yang et al.[118] simulated graphene sheets with a triangular asymmetric array of foreign nitrogen atoms. A maximum thermal rectification of RR ≈ 11% at an average temperature of 300 K was calculated, demonstrating that the heat transport from the low to the high N-atoms region was enhanced.

Loh and Baillargeat[22] used MD simulations to determine the thermal rectification of a single-wall BN nanotube. On the left side of the structure an amorphous carbon plug (aC) was placed inside of the BN nanotube. The scattering at the aC plug was leading to a sort of bottleneck due to the reduced space caused by the existence of the plug. A maximum thermal rectification of around RR ≈ 9% at absolute temperatures between 300 K (heat source) and 290 K (heat sink) was observed with a preferred direction from the pristine side to the aC plug side. When increasing the thermal bias, the phonon–phonon
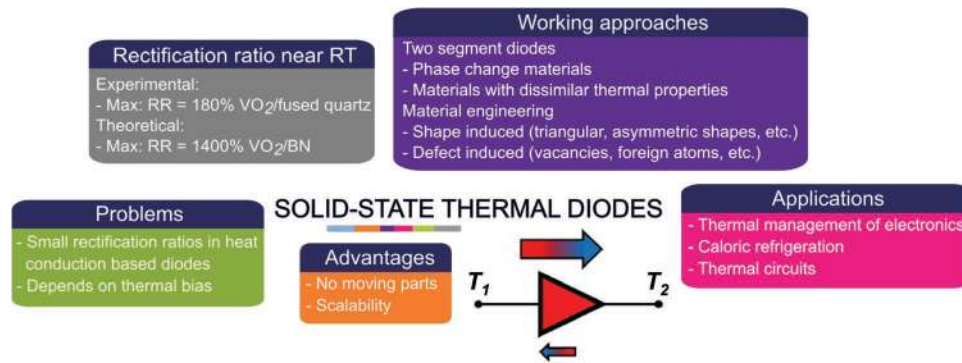
ADVANCED
SCIENCE NEWS
www.advancedsciencenews.com

**ADVANCED
ELECTRONIC
MATERIALS**
www.advelectronicmat.de

Figure 11. Overview of the discussed rectification ratios, working approaches, problems, applications, and advantages of the solid-state thermal diodes.

interaction became dominant, and the scattering at the aC plug became negligible. This led to a lower RR as the thermal bias increased.[22]

Cheng et al.[23] theoretically investigated the thermal transport in a diamond film with a gradient of material grains across the structure. This structure was showing large (growth side) versus small (nucleation side) grains from one side to the other. On the large grain side, the thermal conductivity was mainly dominated by phonon–phonon interactions which involved a reduction of the conductivity with increasing temperature. However, as the size of the grains reduced, the scattering at imperfections and grain boundaries increased. At the small grain side, the thermal conductivity remained almost invariant with increasing temperature. This behavior resulted into a JMT diode like effect. A maximum thermal rectification of RR ≈ 25% for an absolute temperature range between 175 K (heat sink) and 375 K (heat source) was determined using FEM. Similarly, this type of thermal diode could be implemented in other grain gradient microstructures materials.[23]

Similar to the DID structure presented by Wang et al.[34] in Section 2.2.3, Nobakht et al.[19] investigated a graphene sheet with a triangular arranged pore array. In their model, the authors designed a high pore density on the right side of the diode, which gradually decreased as we move to the left side of the diode. Using large-scale atomic/molecular massively parallel simulator (LAMMPS) simulations, the authors observed a higher heat flux from the lower pore density to the right side of the device, achieving a maximum thermal rectification of RR ≈ 78% at room temperature.

2.3. Summary and Comparison of Thermal Diodes

In this section, we presented the different approaches that have been used to develop thermal diodes. Table S1 (Supporting Information) summarizes the most representative parameters for a thermal diode, namely, the RR and the applied thermal bias ΔT. On the one hand, the RR are typically larger in two-segment material devices. On the other hand, the results of material engineered devices are promising for the future progress of this technology and small dimensions applications. For two-segment diodes, PCM can be ideal candidates for use in applications with small thermal biases due to their

sharp thermal conductivity transition, while JMT diodes can achieve larger RR at high thermal biases. This is a key aspect to take that into account when selecting a diode for a particular application.

Generally, solid-state thermal diodes present significantly lower RR than fluidic or mechanical devices.[12] However, nanotechnology has shown enormous potential for further improvement of this technology.[34] Future research projects in the field of thermal rectification should focus on experimental proof of some of the devices reported theoretically.

Figure 11 summarizes the state-of-the-art characteristics of solid-state thermal diodes. Here, the advantages, problems, possible applications, approaches, and rectification ratios are summarized.

3. Thermal Switches

In this section, we present solid-state thermal control devices that are capable to switch between low (off state) and high thermal conductivity (on state).[2] These devices require of an external trigger, i.e., an electric or a magnetic field, pressure, or light, that induces a drastic change in their thermal properties.[2] This unique thermal management capability that diminishes (low k) or facilitates (high k) heat flow across the device would be of great use in heat engines,[2] cryogenics,[120] thermoelectric,[121] refrigeration,[2,122,123] or spacecraft applications.[124]

This part is divided into different sections based on the external parameters that lead to a switch in the thermal properties of the device. Special attention is paid to the following features, which are key performance descriptors of thermal switches:

i. *Switching thermal ratio*: This determines the ability of the device to switch from a low conductivity (off state) to a high conductivity thermal (on state) state. It is mathematically expressed as

$$SR = \frac{\dot{Q}_{on}}{\dot{Q}_{off}} \tag{2}$$

where $\dot{Q}_{on}$ and $\dot{Q}_{off}$ are the heat fluxes in the on and off state, respectively.

**ADVANCED
SCIENCE NEWS**
www.advancedsciencenews.com

**ADVANCED
ELECTRONIC
MATERIALS**
www.advelectronicmat.de

ii. *Characteristic time τ*. This defines how quickly the thermal switch transitions between on/off or off/on states.

3.1. Switching with Electric Field

In this section, we present solid-state thermal switches triggered by an electric field. Ferroelectric materials, i.e., materials that change their electrical polarization due to an external electric field, are potential candidates.[125] A pristine ferroelectric material consists of many domains with a randomly orientated spontaneous polarization, resulting in a net polarization close to zero. When applying an electrical field, domains with a polarization in a similar direction as the direction of the electrical field are aligned with each other. At the maximum polarization, most of the domains are oriented in the same direction. The thermal transport in ferroelectric materials is affected by the domain walls, i.e., domain boundaries, because heat carriers are bound to scatter at them.[126] The boundary scattering is minimized when the domain wall density is at its minimum. This occurs when the electric field is turned on and all domains are oriented in the same direction. Hence, the thermal switch is considered to be in the on state. When turning off the electric field, the domains misalign. This leads to an increased density of domain walls that enhances the scattering of phonons, i.e., reduces the thermal conductivity of the material.[126–128] Then, the thermal switch is considered to be in the off state.[126]

Foley et al.[126] reported a ferroelectric thermal switch made of a thin film $PbZr_{0.3}Ti_{0.7}O_3$ (PZT) membrane presented in **Figure 12**. Figure 12a illustrates the changes of the material due to the switching process. The authors observed an increment of the thermal conductivity with a SR ≈ 1.13 (from $k \approx$ 1.42 W m^{-1} K^{-1} to $k \approx$ 1.61 W m^{-1} K^{-1} at room temperature) by applying an electric field of 100 kV cm^{-1}.[126] This process was reversed by turning off the electric field.[126] Figure 12b presents the thermal conductivity of the switch as a function of time during several cycles. The data show that the switching process did not degrade after several cycles. The authors estimated that the characteristic time was down to $\tau \approx$ 40 ns.[126] Additionally, the authors stated that the magnitude of the electric field

at switching was almost equal to the coercive field of PZT, i.e., the electrical field at which the polarization reverses.[126] This agreed well with the theory that the thermal switching occurs due to phonon scattering at the domain walls. In other words, below an electric field of 100 kV cm^{-1} domains started to shrink, the remaining polarization disappeared, and the thermal conductivity decreased because of the increasing phonon domain wall scattering.[126]

Yigen and Champagne[129] reported the thermal modulation of suspended graphene when doping it using a back-gate electrode. The authors studied the thermal conductivity of suspended graphene at temperatures between 50 and 160 K.[129] The graphene was suspended above a Si/SiO_2 substrate, which acted as a back-gate electrode, while being thermally connected to two gold contacts. A voltage V_G up to 5 V was applied and the electronic thermal conductivity (k_e) was extracted via self thermometry and self-heating methods. An increase of the electronic thermal conductivity by more than a factor of 2 (from around 2 W m^{-1} K^{-1} at $V_G = 0$ V, to above 4 W m^{-1} K^{-1} at $V_G = -5$ V and 100 K) was observed. The authors stated that high-energy carriers are injected into the suspended device and thus the increase of k_e is related with the increase of the charge carrier while the bias is applied.[129]

Additionally, thermal switching has been observed in electrochromic materials, which are specially interesting for spacecraft applications.[130,131] Electrochromic materials can vary their optical properties electrochemically,[132] which also affects their radiative heat transport. Radiative heat transfer is especially important for space applications, where radiation is the only efficient heat transfer mechanism. The thermal management of satellites has to take into account the temperature changes between day and night and changes in solar radiation between the exposed and shadowed position, which could differ up to 2000 W m^{-2}.[133] Demiryont et al.[130,131] developed a thermal switch (EclipseVED), which consists of a multilayer structure containing a transparent electrode, an ion storage layer, an electrolyte layer, an electrochromic layer, and a reflective electrode. When a low voltage (±1 V) was applied, the electrochromic material switched between a colored high emittance state (on) and a bleached low emittance state (off). On the one
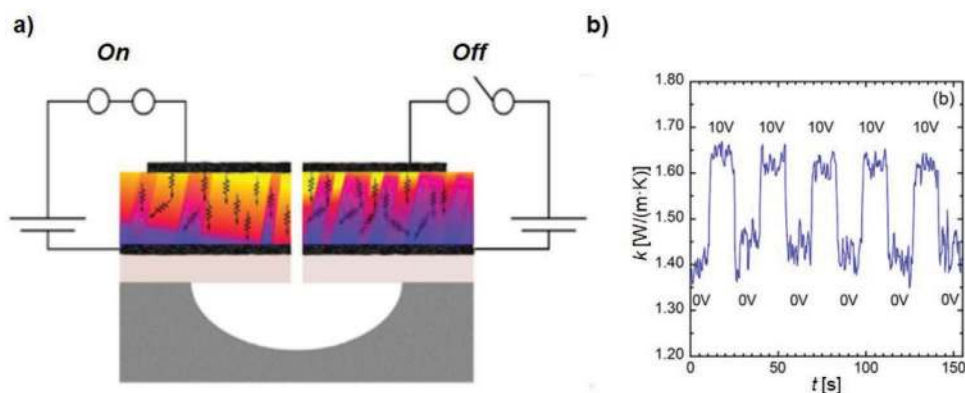

Figure 12. Thermal switching in a ferroelectric thin film investigated by Foley et al.[126] a) Schematic drawing of the structural changes due to domain wall movement when applying an electrical field. When an electric field is applied, the domain wall density decreases (left side). Without electric field, the phonon scattering at the domain walls is increased (right side), and b) thermal conductivity (k) variation as a function of time (t) with electric field for multiple cycles. Reproduced with permission.[126] Copyright 2018, American Chemical Society.

ADVANCED
SCIENCE NEWS
www.advancedsciencenews.com

ADVANCED
ELECTRONIC
MATERIALS
www.advelectronicmat.de

hand, heat was efficiently radiated due to the high emittance of the electrochromic layer in the on state. On the other hand, heat was retained due to the low emittance in the off state.[130] The authors claimed that the emittance of this device can be switched with a SR ≈ 7.7 at a temperature of 300 K.[131] In this particular case, space was considered as the heat sink. Typical electrochromic materials are metal oxides,[134–136] small organic and inorganic materials, or conjugated polymers.[137,138]

3.1.1. Theoretical Predictions of Thermal Switches with an Electric Field

Recently, some theoretical works have been carried out targeting thermal switching effects in ferroelectric materials. Liu et al.[125] used linearized Boltzmann transport equations to predict thermal switching in other ferroelectric materials. In this theoretical work, the authors investigated ferroelectric $PbTiO_3$ (PTO) structures and determined how the thermal conductivity of the material changed under the presence of an electric field. Their results showed that in order to maximize the switching properties of this type of ferroelectric switches, three strategies must be followed: i) use samples with domain sizes larger than the critical domain size; ii) maximize the sensitivity of the domain sizes to an electrical field; and iii) decrease the absolute temperature to maximize the thermal conductivity and increase the switchability.[124] Additionally, Bellido et al.[139] reported on the impact of the domain walls in similar structures, showing promising properties for thermal switches. Liu et al.[140] theoretically investigated thermal switching in $BaTiO_3$ triggered by an electric field. Their results indicated a theoretical maximum switching ratio of 9.4.

3.2. Switching with Magnetic Field

In this section, we present thermal switches triggered by a magnetic field. Several magnetic materials and structures have been explored for thermal switching.[141,142] Some of these thermal switches were observed at low temperature,[120,143] which make them good candidates for cryogenic applications.[143]

Zhao et al.[141] presented a thermal switch based on an antiferromagnetic $Co_3V_2O_8$ single-crystal insulator at low temperatures. This material was used as a thermal switch at temperatures between 6 and 12 K. In this temperature range, magnetic phase transitions occur from a paramagnetic to a commensurate ferromagnetic phase with several intermediate transitions. At the phase transition, phonon scattering was increased by the magnetic excitation of the transition process, which decreased the thermal conductivity.[144] The authors observed that the magnetic ground state can be stabilized by applying a magnetic field up to 14 T. The presence of this magnetic field (on state) reduced the phonon scattering, leading to an increase of the thermal conductivity.[141] This resulted into a maximum SR ≈ 100.

Ferromagnetic materials can also be used for developing thermal switches. In these materials, it is important to take into account that not only phonons and electrons but also magnons transport heat.[145–147] A magnon is a quantized spin wave due to

the exchange interaction of the electron spins in the ferromagnetic material.[148] It can be seen as a quasiparticle, whose properties are strongly dependent on the arrangement of the magnetic moments, the domain wall distribution, and the applied magnetic field. As an example, Huang et al.[149] investigated a thermal switch based on ferromagnetic Ni nanowires. In these ferroelectric structures, when no magnetic field was applied (on state), the total thermal conductivity (k_{total}) could then be expressed as follows

$$\kappa_{total} = \kappa_e + \kappa_{ph} + \kappa_{m\_short} + \kappa_{m\_long} \tag{3}$$

where κ_e is the electronic, κ_{ph} is the lattice, κ_{m_short} the magnonic (with short wavelength) and κ_{m_long} the magnonic (with long wavelength) thermal conductivity contributions. However, when a magnetic field of certain magnitude was applied to the sample, the long wavelength magnons were inhibited from contributing to the net thermal conductivity.[149] This led to a variation of the thermal conductivity of the sample. Under a magnetic field applied (off state), the total thermal conductivity could be expressed as

$$\kappa_{total} = \kappa_e + \kappa_{ph} + \kappa_{m\_short} \tag{4}$$

Therefore, the difference in thermal conductivity between the on and off state was mostly due to the change of long wavelength magnons, i.e., $\Delta k \sim k_{m\_long}$. The authors observed a variation of the total thermal conductivity from $k = 32$ W m^{-1} K^{-1} to $k = 12$ W m^{-1} K^{-1} when applying a magnetic field up to 0.101 T at room temperature. This change is equal to a thermal switching ratio of ≈ 2.7.

Kimling et al.[150] developed a thermal switch based on a nanometer ferromagnetic Co/Cu multilayer structure. The thermal switch was achieved by combining layers of Co followed by Cu layers. In this configuration, an external magnetic field varied the remanent magnetic polarization of the Co layers. When a magnetic field was applied to this multilayer structure, all the Co layers were oriented in a parallel direction so that the spin-up electrons were transported easily along the Co/Cu layer. Under no magnetic field applied, the configuration was antiparallel, and the carrier transport was diminished. As a consequence, the authors observed a variation of the thermal conductivity from $k = 18$ W m^{-1} K^{-1} (antiparallel configuration) to $k = 32$ W m^{-1} K^{-1} (parallel configuration) under a magnetic field of 200 mT.

Dhara et al.[151] explored the tunability of the thermal conductivity of an InAs nanowire field-effect transistor. In their measurements, the authors investigated both the influence of a magnetic and an electrostatic field on the thermal conductivity. The thermal properties were obtained by means of a modified 3ω method while applying a magnetic field and at different gate voltages of the transistor structure at low temperatures between 10 and 50 K. At a gate voltage of −10 V the thermal conductivity was measured to be $k \approx 0.2$ W m^{-1} K^{-1} and at 10 V $k \approx 0.5$ W m^{-1} K^{-1} with SR ≈ 2.5. In the same device, the authors observed a reduction from $k \approx 0.45$ to $k \approx 0.2$ W m^{-1} K^{-1} with SR ≈ 2.3 when applying a magnetic field of 6 T.

Additionally, superconductors have also been proposed for developing low-temperature thermal switches.[143] In this

**ADVANCED
SCIENCE NEWS**

www.advancedsciencenews.com

**ADVANCED
ELECTRONIC
MATERIALS**

www.advelectronicmat.de

particular case, the thermal switching occurs when an external magnetic field above the critical field of the superconductor is applied. In pure metal superconductors, e.g., Sn or Pb, a switching ratio of above SR ≈ 100 could be achieved at temperatures below 1 K.[143]

3.2.1. Theoretical Predictions of Thermal Switching with a Magnetic Field

Latella and Ben-Abdallah[152] theoretically calculated the thermal resistance changes of a linear InSb nanoparticle chain. A thermal gradient was set along the chain and the structure was investigated at room temperature using a Landauer-like formalism. The radius of the nanoparticle was set to be 100 nm with 200 nm distance between two particles. The authors observed an increase of the thermal resistance by almost a factor of 2 when a magnetic field of 2 T was applied to it (SR ≈ 2). The authors stated that the change of thermal resistance was due to a shift of the resonant heat transfer modes.

3.3. Switching with Pressure/Strain

In this section, we present thermal switches triggered by a change in the external pressure or due to strain. When an external pressure is applied to the material, it can induce a phase change that leads to changes in the thermal properties of the material. As an example, Talyzin et al.[153] worked on the phase transition in mm sized LiBH$_4$ structures through the application of high pressure (≈1 GPa). The authors observed that the thermal conductivity switched by a factor of 2–3 when the pressure was varied from 1 to 0.5 GPa. This is due to a material phase transition that happens at ≈0.7 GPa, which led to an increase of the thermal conductivity from $k ≈ 1.5$ W m^{-1} K^{-1} to $k ≈ 3.5$ W m^{-1} K^{-1}. Using these values, a switching ratio of ≈2.3 was obtained.

Similarly, McGuire et al.[154] proposed a pressure thermal switch based on the B1 (face-centered cubic) to B2 (body-centered cubic) phase transition in NaCl.[154] Originally, this structure was not presented as a thermal switch, but the data of the changes in the thermal conductivity were equal to a switching ratio of ≈1.6.[154]

Zeng et al.[155] investigated the thermal conductivity in strained multilayer graphene. The authors measured the thermal conductivity as a function of an applied tensile strain. The thermal conductivity decreased from $k ≈ 551$ W m^{-1} K^{-1} in the unstrained state to $k ≈ 395$ W m^{-1} K^{-1} at a tensile strain of 1%, which is equal to a SR ≈ 1.4. The authors stated that the reduction of thermal conductivity was related to an increased phonon-grain boundary scattering induced due to the strain.[155]

3.3.1. Theoretical Predictions of Thermal Switching with Pressure/Strain

Liu et al.[156] theoretically evaluated a switchable graphene structure triggered by an external pressure. The authors investigated a single-layer graphene device which is partly sandwiched by two clamps in the center of the layer. The distance between the two clamps was adjusted due to the external pressure. The authors used MD simulations to evaluate the difference in the heat flux depending on the applied pressure. The heat flux was induced due to a heat source and heat sink located at the two ends of the graphene layer. By applying an external pressure of 50 GPa a switching of the heat flux with a factor of up to SR ≈ 1.5 was observed. The authors claimed that the external pressure induced a change in the phonon dispersion relation of the clamped region. As a result, phonon scattering at the interface of the clamped/nonclamped region occurs, leading to a reduced heat flux.

Gao et al.[157] investigated a switchable MoS$_2$/Graphene Bilayer heterostructure triggered by an external strain using LAMMPS simulations. The authors calculated the thermal conductivity in a heterostructure consisting of a single layer of graphene and a single layer of MoS$_2$ with a spacing of 0.335 nm between layers. First, the heterostructure was equilibrated at 300 K. Then a uniform stretching was induced along the x-direction. A heat flux was obtained by applying a temperature gradient from 320 K at the heat source to 280 K at the heat sink. In the unstrained case, a thermal conductivity of around 34 W m^{-1} K^{-1} was predicted. At a strain of 15% the predicted thermal conductivity reduced to 18 W m^{-1} K^{-1}, which would result in a SR ≈ 1.9. The authors claimed that the application of the strain was leading to a shift of the phonon frequency from high to low modes, which resulted in the decreased thermal conductivity.

3.4. Switching with Light

In this section, we present a polymer thermal switch, triggered by a light stimulus. Polymers are attractive materials for thermal management given their possibilities to tune their thermal conductivity with doping,[158] porosity,[159] size,[160] or chain orientation,[161] among others. Additionally, polymers can change their structures due to external stimuli. As an example, Shin et al.[162] reported for azobenzene polymer a change of structure from a planar (*trans*) to a nonplanar (*cis*) in response to UV light stimuli. The whole switching process is illustrated in **Figure 13**. In Figure 13a,b the structural change of this polymer thermal switch is illustrated. When radiating the sample with an UV light (wavelength of 375 nm), the polymer switches from its *trans* to its *cis* structure. However, by radiating the polymer with green light (wavelength of 530 nm), the polymer switches back to the *trans* structure. Figure 13c shows how the thermal conductivity of the polymer changes under these stimuli. The authors measured thermal conductivity changes from $k ≈ 0.35$ W m^{-1} K^{-1} to $k ≈ 0.1$ W m^{-1} K^{-1}, i.e., SR of ≈3.5. Figure 13d shows several thermal switching cycles, indicating that this process was reversible. The characteristic switching times were estimated to be $\tau ≈ 10$ s.

3.5. Summary and Comparison of Thermal Switches

In Section 3, we presented the recent progress in solid-state thermal switches. Table S2 (Supporting Information) compares the most important features of the thermal switches
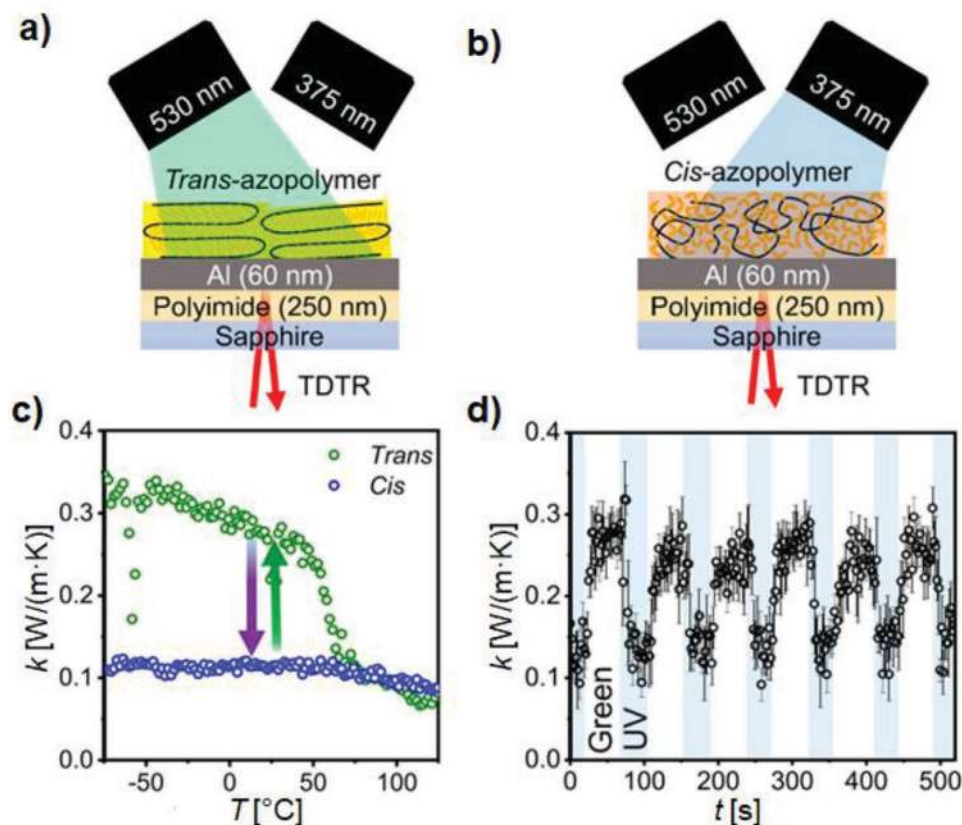
Figure 13. Thermal switching in azobenzene polymers investigated by Shin et al.[162] a,b) The polymer changes its structure (*trans* vs *cis*) under UV or green light stimuli; thermal conductivity (*k*) variation of the *trans* and *cis* structures c) as a function of the temperature (*T*) and d) as a function of time (*t*). Adapted with permission.[162] Copyright 2019, PNAS.

presented in this section, like switching ratios, temperature of application, and type/magnitude of the external trigger applied. High SRs can be obtained at low temperatures in magnetic materials, which is especially interesting for cryogenic applications.

In comparison to fluidic and especially mechanical devices,[12] the SRs for solid-state thermal control devices under ambient conditions are still relatively low. The SR values for solid-state devices typically start from below 2 (ferroelectric PZT[126] or Co/Cu Multilayer[150]), to values between 2.5 and 3.5 (Ni nanowires[149] or azobenzene[162]) up to values above 5 (e.g., electrochromic materials[130,131]). In fluidic thermal switches at ambient conditions, SR values start below 2 (electrically/magnetically induced anisotropy in liquid crystals[163,164]), to higher values typically around 10–50 (fluidic bridge thermal switch with glycerol[165] or nanofluids[166]) and above (fluidic bridge thermal switch with galinstan and vaporized NaOH[167] and electrically induced jumping water droplets in air[168]). In mechanical devices, SR values start around 2 (thermal switch based on electromechanical effect in aluminium film[169]), can overcome SR = 20 in some cases (thermal switch based on electromechanical effect in parylene C[170]), or SR ≤ 1000 in some particular cases (thermal switch based on electromechanical effect in polypropylene film[171]).

However, the recent progress of the field over the recent decade shows a high potential for further improvement. Future thermal switches need to be designed to maximize the SR and characteristic time by considering new material structures and strategies.[139] An improvement in the properties of solid-state thermal switches is key to use them for thermal management applications.

Figure 14 shows key aspects of the reviewed solid-state thermal switches of this section. Hereby the advantages, problems, possible applications, materials, switching times, and switching ratios are summarized.

4. Thermal Regulators

In this section, we present solid-state devices for thermal regulation. The thermal properties of thermal regulators are modified with temperature.[172] In these devices, the thermal conductivity of the material changes when a critical transition temperature, T_{crit}, is reached. This is typically due to a change of the material crystal structure.[172] PCMs are the main class of thermal regulators, since their change of phase at certain temperature leads to a variation in their thermal properties.[172,173] In this section, we review different types of solid-to-solid PCMs that can be used as thermal regulators. This type of device can be integrated in electronics to prevent overheating,[2] as well as in other applications, such as cryogenics,[174] phononic data processing,[10] or thermal energy storage.[173]
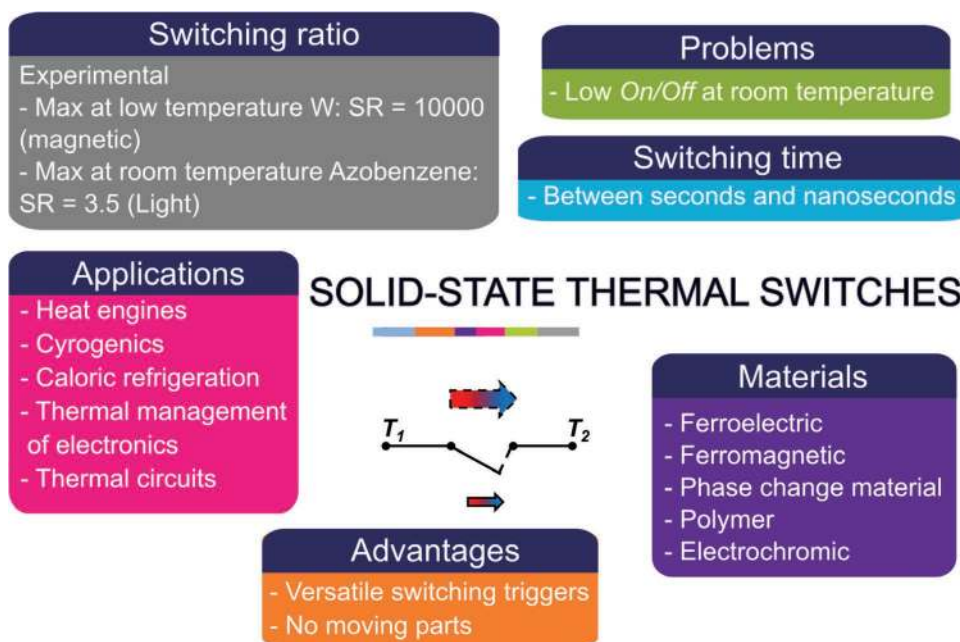
Figure 14. Overview of the discussed switching ratios and times, working materials, problems, applications, and advantages of solid-state thermal switches.

First, we review thermal regulators based on solid-to-solid metal alloy phase changes. Second, we present MIT solid-state thermal regulators based on VO_2. Special attention is paid to the following features, which are key to determine the performance of thermal regulators:

i. *Switching thermal regulation ratio*: The definition is the same as the SR explained for thermal switches in Equation (2).

ii. *Characteristic time* (τ): This defines how quickly the thermal properties of the regulator vary at the transition temperature.

4.1. Thermal Regulators Based on Metal Alloys

Compounds of base metals,[175] known as metal alloys, exhibit solid-to-solid phase change. They show potential to modulate their thermal properties for thermal regulation applications. As an example, Zheng et al.[176] reported thermal regulation in Mn_xMGe (M = Co, Ni, $0.98 < x < 1.02$) alloys that transform from a martensitic to an austenitic phase between 300 and 600 K depending on the material composition. This phase change resulted in the formation of twin boundaries, i.e., grain boundaries that were oriented in parallel. These twin boundaries contributed to the scattering of heat carriers, leading to a reduction of the thermal conductivity. The authors reported a maximum switching of the thermal conductivity from $k \approx 11$ W m^{-1} K^{-1} to $k \approx 15.5$ W m^{-1} K^{-1} (SR $\approx$ 1.4) for $Mn_{1.014}NiGe$ with a phase transition temperature at near $T_{crit} \approx 600$ K. Additionally, the authors also observed thermal switching behavior in $Mn_{1.007}CoGe$, with a thermal conductivity variation from $k \approx 7$ W m^{-1} K^{-1} to $k \approx 8.5$ W m^{-1} K^{-1} and corresponding SR $\approx$ 1.21. These results show major improvements compared to previous investigated metal alloys, such as NiTi.[177]

Recently, Zheng et al.[172] also presented new types of thermal regulators based on polycrystalline Ni-Mn-In Heusler alloys, whose thermal regulation working principle was similar to the one explained above. In these structures, the phase transition occurred between 320 and 370 K. As shown in **Figure 15**a, the authors observed reversible switching of the thermal conductivity from $k \approx 7.5$ W m^{-1} K^{-1} to $k \approx 13$ W m^{-1} K^{-1} with SR $\approx$ 1.75. Moreover, the authors calculated the average logarithmic rate of change in thermal conductivity in a certain temperature range as $Z = \dfrac{(\partial \ln(k))}{(\partial \ln(T))}$ for Ni-Mn-In alloys in comparison to other materials.[172] This parameter gives an indication on how fast a change in the thermal conductivity occurs.[172] The Z values of Ni-Mn-In alloys and other materials are presented in Figure 15b.

4.2. Thermal Regulators Based on VO_2

As explained in Section 2.1.2, VO_2 is one of the well-known solid-to-solid phase change materials. VO_2 can be used as a component in thermal diodes as discussed earlier, but also as a thermal regulator, taking advantage of its insulator-to-metal phase change transition at a temperature of $T_{crit} \approx 340$ K.

Dahal et al.[178] developed a thermal regulator based on a vanadium (V) core surrounded by a VO_2 shell (V-VO_2 core shell) which is schematically shown in Figure 15c. The structures are thermally insulating below $T_{crit} \approx 340$ K, due to the insulating VO_2 shell. However, above the transition temperature, free electrons can be transferred from the metallic V core to the metallic VO_2 shell. Since the electrons are heat carriers, this resulted in a higher thermal conductivity. On the one hand, changes in the electronic component of thermal
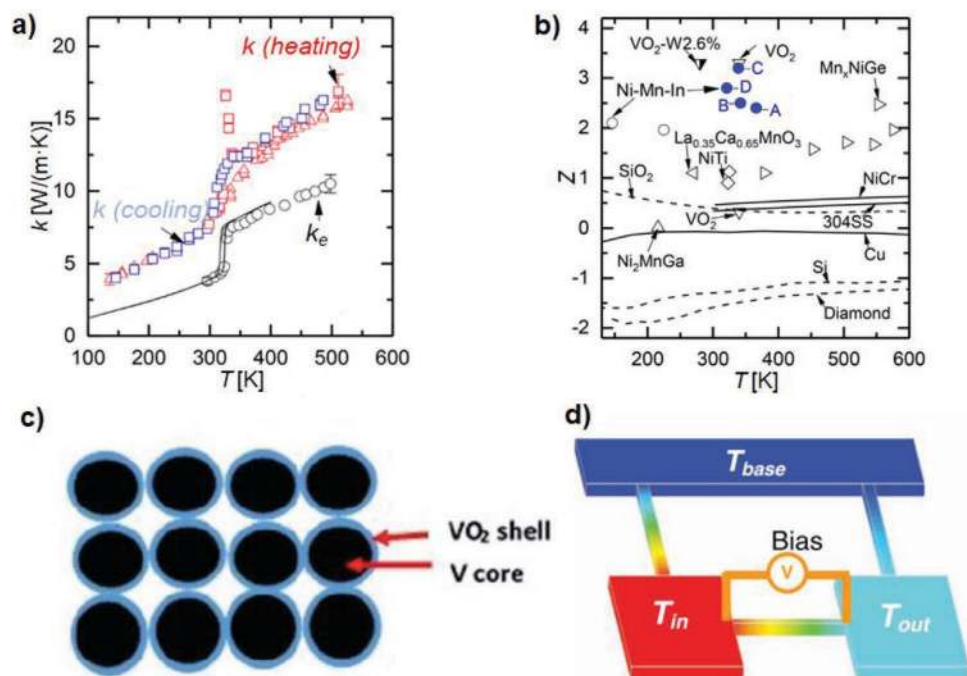
**ADVANCED
SCIENCE NEWS**
www.advancedsciencenews.com

**ADVANCED
ELECTRONIC
MATERIALS**
www.advelectronicmat.de

Figure 15. Thermal regulation in different structures. a) Thermal conductivity (k) of the Ni-Mn-In alloy investigated by Zheng et al.[172] as a function of the temperature (T) during the heating and cooling processes, b) average logarithmic rate change (Z) versus T for a selection of materials including Ni-Mn-In alloy samples (point A–D). Reproduced with permission.[172] Copyright 2019, Advanced Engineering Materials. c) schematic image of the VO_2/V core–shell structure investigated by Dahal et al.[178] Reproduced with permission.[178] Copyright 2017, RSC Advances. d) Schematic drawing of the VO_2 nanobeam thermal regulator device developed by Xie et al.[173] Reproduced with permission.[173] Copyright 2011, Advanced Functional Materials.

conductivity were relatively high (from $k_e \approx 1.5$ W m^{-1} K^{-1} to $k_e \approx 4.5$ W m^{-1} K^{-1}). On the other hand, the lattice component of the thermal conductivity decreased at the same time (from $k_{ph} \approx 6.5$ W m^{-1} K^{-1} to $k_{ph} \approx 4.5$ W m^{-1} K^{-1}). This led to a rather small change in the total thermal conductivity, with a maximum SR ≈ 1.22.

Another approach was reported by Xie et al.,[173] who proposed a single-crystalline VO_2 nanobeam structure to achieve controlled thermal regulation. Figure 15d shows the VO_2 nanobeam connecting an input terminal T_{in} as a heat source to an output terminal T_{out} as a heat sink. Both terminals are connected to the substrate with the temperature (T_{base}). When the input terminal is heated up, the heat flows to the output terminal across the nanobeam and to the substrate. When the input temperature reaches $T_{crit} \approx 340$ K, the phase of the VO_2 nanobeam changed from insulating to metallic, resulting in a sharp increase of T_{out}. The authors obtained a high and a low temperature state in the output terminal which was regulated due to the phase change.[173] Under this configuration, the VO_2 nanobeam can work as a thermal memory. The authors observed a SR ≈ 1.07 in the nanobeam when reaching $T_{crit} \approx 340$ K with a characteristic time of $\tau \approx 4$ s. This effect, the authors applied a bias between the two terminals, as shown in Figure 15d. The authors observed an enhancement of the switching ratio and a reduction of the phase change transition temperature. The electronic contribution to the thermal transport was significantly higher than before so that the impact in the total thermal conductivity was higher as well.

4.3. Thermal Regulators Based on PE Nanofibers

Zhang and Luo[179] proposed the use of PE nanofibers to develop a thermal regulator. PE nanofibers can change their phase from an ordered to a disordered system when reaching a transition temperature.[76] Using NEMD simulations on a PE nanofiber chain, the authors reported a SR ≈ 5 due to a phase transition at around $T_{crit} \approx 400$ K. Additionally, the simulation was repeated under strained conditions, showing that the initial thermal conductivity of PE nanofibers can be adjusted from $k \approx 10$ W m^{-1} K to almost $k \approx 50$ W m^{-1} K^{-1}.

Recently, such a thermal regulation was investigated experimentally by Shrestha et al.,[180] where the authors showed promising properties of PE nanofibers for thermal regulation. In this case, the thermal conductance of the fiber is regulated with switching ratios up to 10 and the transition occurs at temperatures above $T_{crit} \approx 400$ K.

4.4. Summary and Comparison of Thermal Regulators

In Section 4, we presented the recent progress in solid-state thermal regulators. Table S3 (Supporting Information) summarizes the most important features of the thermal regulators presented in this review, like the SR, working temperature (i.e., the range of temperature in which the regulator can work), and the transition temperature (T_{crit}). While VO_2 is an often-considered material for thermal regulation purposes, the Heusler alloys reported by Zheng et al.[172] present one of the

**ADVANCED
SCIENCE NEWS**

www.advancedsciencenews.com

**ADVANCED
ELECTRONIC
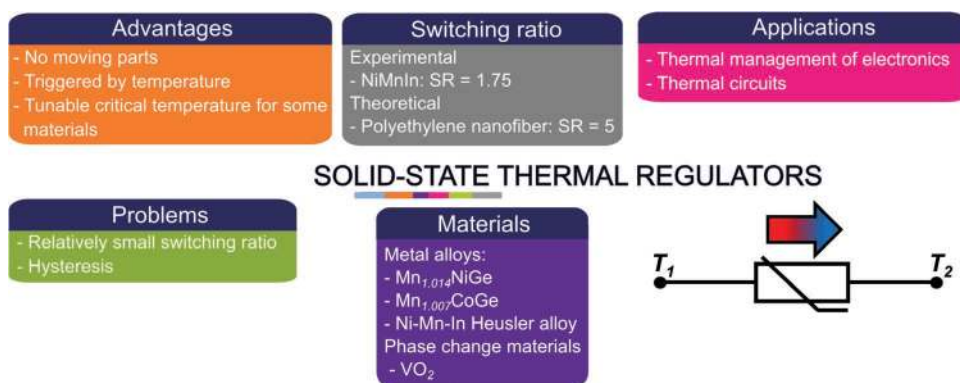MATERIALS**

www.advelectronicmat.de

Figure 16. Overview of the discussed switching ratios, working materials, problems, applications, and advantages of solid-state thermal regulators.

largest thermal regulation ratios to date near room temperature. Recently, Shrestha et al.[180] showed high thermal regulation in PE nanofibers at temperatures above 400 K. However in comparison to fluidic and mechanical devices where switching ratios above 100 were obtained, these SRs (usually below 2) are still moderate.[12] While the ability to modulate the thermal conductivity in solid-state thermal regulators and switches holds great promise to develop a novel thermal technology, like heat logic,[10] future work must focus on enlarging the SR using new phase change materials or strategies. As an example, silver sulfides and silver selenides are materials that could also be used for thermal regulation purposes.[53,181] Others like pentaerythritol,[182] manganese,[183] or $Ge_2Sb_2Te_5$[184,185] could also lead to highly switchable thermal devices. Those materials might be the base for further research to develop new solid-state thermal regulators.

Figure 16 shows the key aspects of the solid-state thermal regulator devices that have been discussed in this section. Here we consider the switching ratios, the used materials, possible applications, advantages, and problems.

5. Thermal Transistors

In this section, we present the recent developments of solid-state thermal transistors. While in a thermal switch we have two distinct on and off states, thermal transistors typically allow a higher modulation of the thermal conductivity of the sample.[186] Strictly speaking, the thermal transistors reported here do not amplify the heat flow with the gate, as their electrical counterparts can do with electrical signals, but they work more like modulators for heat.[186] Thermal transistors are the holy grail component for thermal management applications that require a more dynamic control.[187] For example, thermal transistors (as thermal switches) could be used in batteries to avoid overheating[188] or as a thermostat in a car.[189] When the car battery is cold the thermal transistor remains off to retain energy.[189] When the car battery is overheating the thermal transistor is turned on to facilitate the heat dissipation and to maintain an optimal operating temperature.[189] Another example of usage could be in phase change energy storage elements, between the storage element and the heat source. When the heat source is active, the thermal transistor could be

in a thermally conductive state, which allows the phase change material to absorb heat rapidly. Once the energy is stored via the phase change, the thermal transistor could change to an insulating state. Additionally, the solid-state thermal transistor is a key element to develop future thermal technology based on heat logic (thermal computers).[9,189,190]

This section focuses mainly on electrochemical thermal transistors, as this is one of the most popular approaches to modulate the thermal conductance across the material. It is worth noting that some of the thermal switches presented in Section 3 could be categorized as thermal modulators. However, we believe that the devices presented in this section are better categorized as transistors because of the more continuous thermal modulation in comparison to the strict separation of thermal states characteristic of switches. Special attention is paid to the following features, which are key to determine the performance of thermal transistors:

i. *Switching thermal ratio*: The maximum achievable difference between the lowest and highest possible heat flux across the device. This is equally defined as the SR in Equation (2).

ii. *Characteristic time* τ: The time needed to change the thermal conductivity from its maximum to its minimum value, and vice versa.

5.1. Thermal Transistor Based on Li_xCoO_2

Cho et al.[191] proposed a Li_xCoO_2 structure with a reversible lithiation intercalation process that can work as a thermal transistor. The results of this publication are presented in **Figure 17**. Figure 17a illustrates this device, where the electrochemical cell consists of a 500 nm thick $LiCoO_2$ cathode and a Li counter electrode. $LiCoO_2$ was used because of its reversible lithiation characteristics. The liquid electrolyte in between the electrodes was composed by 1:1 ethylene carbonate and dimethyl carbonate containing 1 M $LiClO_4$. Sapphire was used as the substrate because of its optical transparency and high thermal conductivity, which assured a low temperature rise during the measurement of the thermal conductivity with time-domain thermoreflectance (TDTR).[191] The Al layer worked as thermal transducer and the SiO_2 layer acted as a thermal insulator between Al and sapphire. The $LiCoO_2$ was annealed at 500 °C to maximize its discharge capacity. During the charging
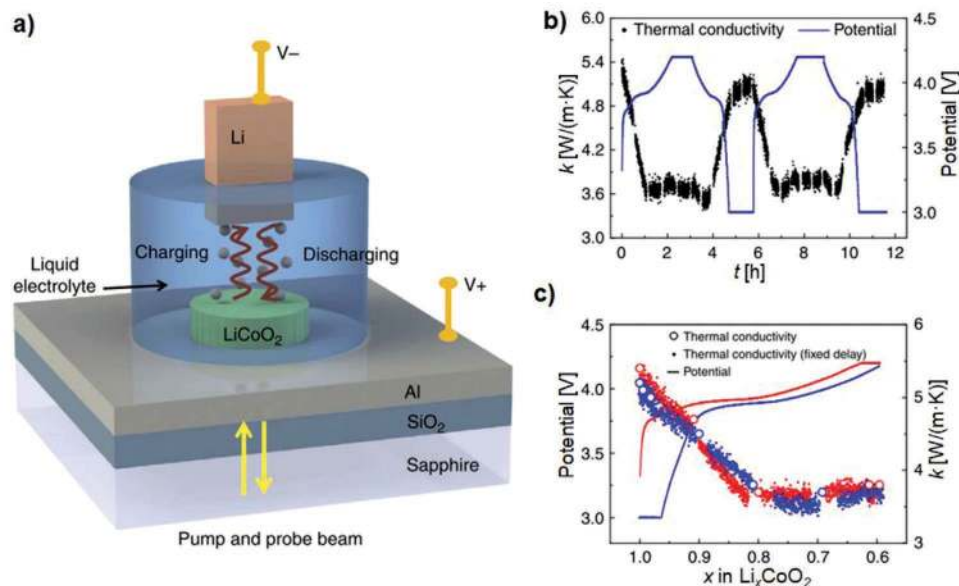
**ADVANCED
SCIENCE NEWS**
www.advancedsciencenews.com

**ADVANCED
ELECTRONIC
MATERIALS**
www.advelectronicmat.de

Figure 17. Li_xCoO_2 thermal transistor investigated by Cho et al.[191] a) Schematic drawing of the thermal transistor, b) thermal conductivity (k) and potential of Li_xCoO_2 during two complete cycles of delithiation and lithiation as a function of time (t) and c) as a function of the Li content (x). Reproduced with permission.[191] Copyright 2014, Nature Communications.

process, the Li content of Li_xCoO_2 was decreasing to a value of $x = 0.6$. The electrochemical cell was cycled between a working voltage V_{WE} 3 and 4.2 V, while after each charge/discharge step the potential was held constant for 1 h.

Figure 17b shows the potential and the thermal conductivity variation during different charging and discharging cycles. During the charging process the cross-plane thermal conductivity decreased from a value of $k \approx 5.4$ W m^{-1} K^{-1} to $k \approx 3.7$ W m^{-1} K^{-1}. This is equivalent to a maximum SR ≈ 1.5, while the characteristic time was $\tau \approx 6$ h. Figure 17c shows the potential and thermal conductivity as a function of the Li content x during the electrochemical reaction. As the Li content reduced, the thermal conductivity decreases until it saturated for values below 0.8. In order to explain this behavior, the authors considered two plausible explanations: i) Li_xCoO_2 has two phases with two different thermal conductivities; ii) the phonon scattering is increased due to Li-vacancies in the charged state.

5.2. Thermal Transistor Based on Black Phosphorus (BP)

Kang et al.[192] proposed a bulk black phosphorus sample in an electrochemical bath to control the thermal conductance via Li ion intercalation as illustrated in **Figure 18**. Black phosphorous has a high specific capacity for ionic Li intercalation,[193] which makes it a good candidate for developing an electrochemical thermal transistor. Similar to the $LiCoO_2$ transistor of Section 5.1, this structure is suitable for charging and discharging of the phosphor electrode using Li. Figure 18a illustrates the black phosphorus thermal transistor, where the Li electrolyte is located between the two electrodes, i.e., BP and Li. The authors measured the thermal properties of the BP via TDTR. Under this configuration, Li ions were reversibly intercalated into the BP.

The results of the cross-plane thermal conductivity (k_c) as a function of Li content x and as function of the cycle number is shown in Figure 18b,c, respectively. The authors claimed that the foreign Li atoms acted as phonon scattering centers, leading to a thermal conductivity decrease as the Li content increased. The maximum switching ratio was SR ≈ 1.6 which is slightly higher than in the Li_xCoO_2 transistor presented in Section 5.1. In order to reach an equilibrium, a long waiting time between the steps was chosen, resulting in a characteristic time of $\tau \approx 36$ h. Nevertheless, this characteristic time could be lower by reducing the time between steps.

5.3. Thermal Transistor Based on Thin MoS₂ Films

Sood et al.[187,194] reported a thermal transistor based on the lithiation and delithiation processes of a 10 nm thick MoS_2 film as illustrated in **Figure 19**. Figure 19a illustrates the setup and the electrochemical cell used for developing such device. A lithium pellet was used as the reference electrode while MoS_2 was used as the working electrode. These two are immersed in a $LiPF_6$ electrolyte. Figure 19b shows that the Li ions intercalate between MoS_2 layers during lithiation and that the Al layer on top of this material was used as a transducer for TDTR measurements. The Li content x in the MoS_2 was adjusted from pristine ($x = 0$) to fully lithiated ($x = 1$). Figure 19c,d shows the variation of the thermal conductance G during lithiation and delithiation process over time and in terms of Li content x, respectively.

The characteristic time was $\tau \approx 14$ min which is drastically lower in comparison to the transistors presented before. Additionally, the switching ratio was SR ≈ 10, being one of the highest thermal ratios reported to date for solid-state thermal transistors (and switches).[187] The authors carried out NEMD
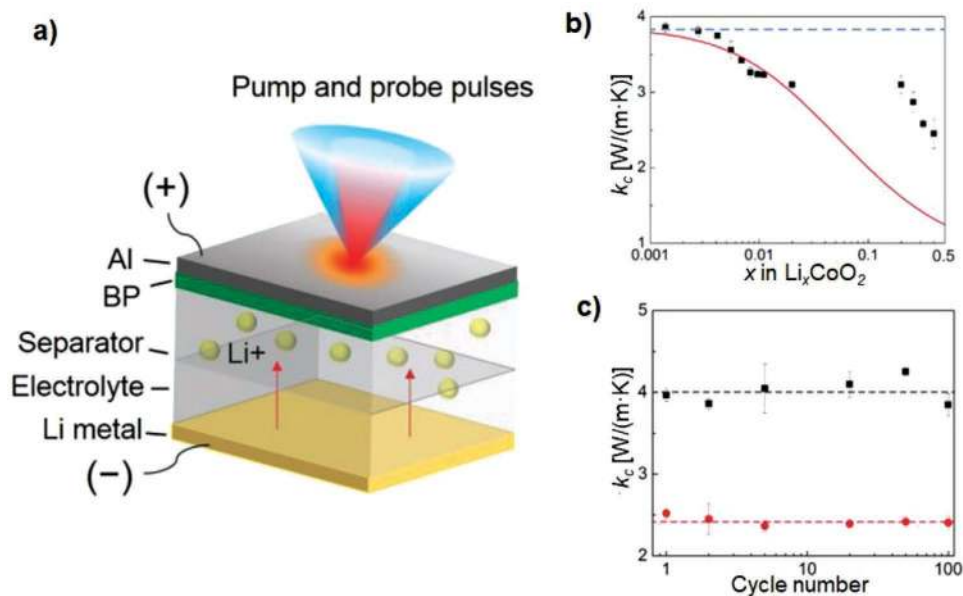
ADVANCED
SCIENCE NEWS
www.advancedsciencenews.com

ADVANCED
ELECTRONIC
MATERIALS
www.advelectronicmat.de

Figure 18. Black phosphorous thermal transistor investigated by Kang et al.[192] a) Schematic drawing of the BP thermal transistor, b) cross-plane thermal conductivity (k_c) as a function of the Li content (x) while discharging (solid rectangular symbols are experimental data, solid line is fitting), c) k_c of the full charged state at a working voltage of $V_{WE} = 2$ V (black squares) and at $V_{WE} = 0.78$ V (red circles) as a function of the cycle number. Reproduced with permission.[192] Copyright 2017, American Chemical Society.

simulations of the steady heat flux across the Li_xMoS_2 film in order to understand the fundamental reasons for the reduction of the thermal conductance with increasing x. Based on these results, the authors considered three mechanisms for such behavior: First, the Li atoms act as phonon rattlers, enhancing the phonon scattering and reducing phonon lifetime.[187,195] Second, the intercalation of the Li atoms leads to a strain in

c-axis, which reduces the group velocity (v) of the phonons. Third, it is assumed that the MoS_2 lattice is stacked by so-called 2H-MoS_2 phase layers in the unlithiated state. Due to the lithiation, the lattice structure changes and is stacked alternating by a 2H-$LiMoS_2$ and a 1T-$LiMoS_2$ layer. Zhu et al.[196] stated that the disorder created due to the coexistence of these two layers results in a reduction of thermal conductivity in MoS_2. These
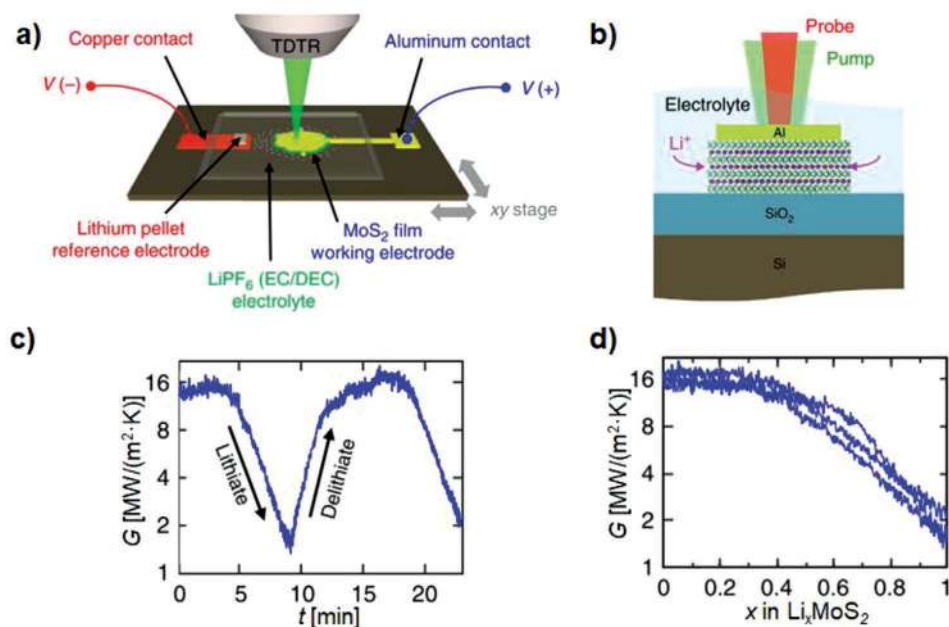

Figure 19. MoS_2 thermal transistor investigated by Sood et al.[187] a) Schematic drawing of the Li_xMoS_2 thermal transistor, b) cross-section view along the MoS_2 lithiated sample, thermal conductance (G) of the Li_xMoS_2 during the electrochemical reaction as a function of c) the reaction time (t) and d) the Li content (x). Reproduced with permission.[187] Copyright 2018, Nature Communications.

**ADVANCED
SCIENCE NEWS**
www.advancedsciencenews.com

**ADVANCED
ELECTRONIC
MATERIALS**
www.advelectronicmat.de

three mechanisms are believed to explain the big difference in the thermal conductance observed experimentally between the lithiation and delithiation states.[187]

5.4. Thermal Transistor Based on SrCoO$_x$

Lu et al.[197] presented an electrochemical cell with tunable thermal conductivity based on the phase transition of SrCoO$_x$. The authors showed that a phase change of brownmillerite SrCoO$_{2.5}$ (BM-SCO) to perovskite SrCoO$_3$ (P-SCO) can be induced by applying an anodic bias. But also, the authors observed a phase change from BM-SCO to a hydrogenated H-SrCoO$_{2.5}$ (H-SCO) phase by applying a cathodic bias. In their setup, the authors deposited a thin film BM-SCO on an yttria-stabilized zirconia (YSZ) substrate via pulsed laser deposition (PLD). The authors used an ionic liquid as the electrolyte and a Pt wire as the counter electrode for the electrochemical cycling. As a part of their project the authors demonstrated that the thermal conductivity was tuned from $k \approx 1.70$ W m^{-1} K^{-1} in BM-SCO to $k \approx 4.33$ W m^{-1} K^{-1} in PV-SCO which is equal to a switching ratio of ≈2.5.[197] In H-SCO, the authors measured an even lower thermal conductivity of $k \approx 0.44$ W m^{-1} K^{-1}.

The authors claimed that the changes in thermal conductivity are caused by the changes in the oxygen stoichiometry, lattice constant, and lattice symmetry, while the influence of the electrical changes on the thermal conductivity is comparable small.[197] In SrCoO$_x$ oxygen vacancies acted as traditional defects. Thus, in the BM-SCO the higher amount of oxygen vacancies induces an increase in phonon scattering. BM-SCO has a higher lattice constant than PV-SCO. The authors claimed that the resulting lattice expansion is leading to a decrease in thermal conductivity in the BM phase.[197] Moreover, the authors hypothesized that PV-SCO should have the highest thermal conductivity due to its high lattice symmetry. A higher lattice symmetry leads to a constriction of the phonon scattering space.[197,198] Finally, the initial oxidation step from BM-SCO to P-SCO can be achieved within a minute, while the reversed step took longer.[197] Further research will be required to determine the exact cycling time in this particular material. In a different research project, a phase transformation from H-SCO to BM-HSCO and from P-SCO to BM-SCO was achieved with a transformation time of 38 min in both cases.[199]

5.5. Summary and Comparison of Thermal Transistors

In this section, we showed that electrochemistry presents an enormous potential to develop thermal transistors. Table S4 (Supporting Information) summarizes the most important features of the thermal transistors working at room temperature and presented in this review, like SRs, switching times τ, type and thickness of the materials used. The largest SR and fastest cycle time to date were achieved for the MoS$_2$ sample.[187] As the authors claimed, the switching ratio of ≈10 observed for this thermal transistor represents an important advance in the field. As an example, the inclusion of these thermal devices in power electronics could avoid failure due to temperature oscillations. First-order calculations suggested that their MoS$_2$ thermal transistor will reduce the temperature swing in a device by 10×, and increase its lifetime by ≈3000×.[187] Although this is very promising, the thermal characteristic times are still moderate ($\tau \approx 14$ min full cycle time). Future work should focus on developing thermal transistors with faster cycling times to respond better to the fast heat flux transients found in electronic devices.

Figure 20 summarizes key aspects of the solid-state thermal transistors reviewed in this section, like switching ratios/time, materials used, advantages/problems, and possible applications.

6. Future Work and Outlook

Solid-state thermal control devices represent an emerging field that could make the leap into advanced heat control, expanding our thermal management capabilities or developing new thermal technology, like computing using heat logic. However, one of the limiting factors of these thermal devices is related to their characteristic performances.[12]

In order to make progress in this field, solid-state thermal control devices should reach performances much higher than those observed to date. Nanotechnology has contributed to
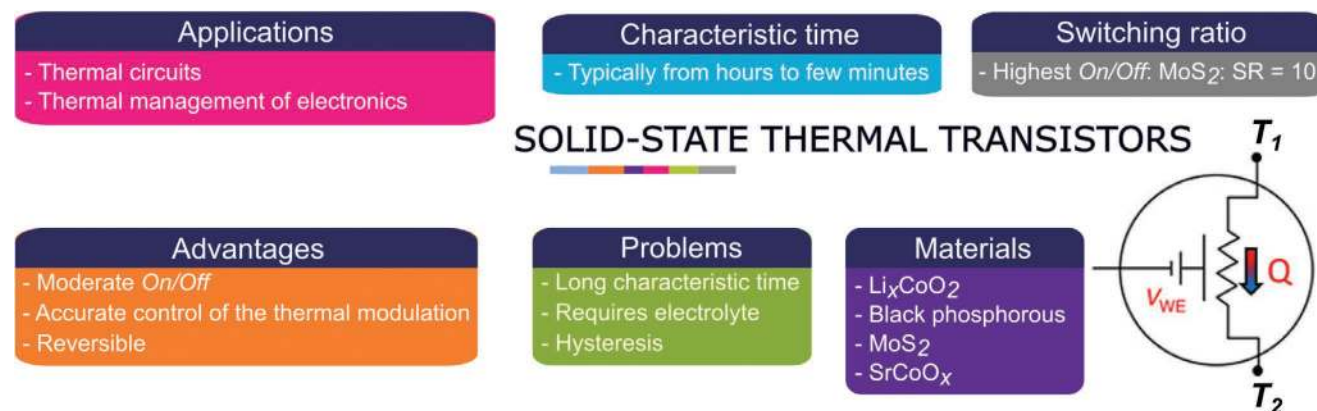

Figure 20. Overview of the discussed switching ratio, characteristic time, problems, applications, and advantages of solid-state thermal transistors. Thermal transistor diagram reproduced with permission.[187] Copyright 2018, Nature Communications.

2000625 (22 of 28)

develop devices based on materials with exciting thermal properties, like graphene or hBN. Nanotechnology is expected to keep on playing a key role in this field by developing materials with tuned thermal properties and new device designs for advanced thermal control. Additionally, the combination of some thermal control methods explained in this review could be explored to bring new opportunities in the field. For future progress, it is also important to account on theoretical approaches for designing novel thermal devices with improved performances. Although some of them have been presented in the theoretical subchapters, we need to create and study new conceptual solutions for high-performance thermal devices that are simulated in high-performance computing environments and experimentally validated for specific applications and their conditions.

Another important factor that must also be addressed is related with the scalability of these thermal components for optimum integration in certain applications. On the one hand, thermal control devices in the nano or microscale are desired for local heat control, like thermal management of electronic components.[2,29,93] On the other hand, these devices should also be scalable to larger sizes to facilitate integration in other applications. As an example, thermal switches or diodes could be integrated in caloric energy conversion systems to enhance the power density by fast and oscillating heat transfer from/to the caloric material and the heat source/sink, but their sizes must be typically larger than the nanoscale.[123,200] Macroscopic or microscopic thermal diodes could solve the remaining problem of unwanted heat diffusion, in, e.g., thermoelectric heat pumps for heating and cooling.[2] The same applies to thermal switches or thermal transistors, which could provide an important advantage for future high power density, ultra-high temperature thermal storage systems adapted to charge or discharge the system between the heat source and sink. An example of giant surface thermal diode systems is their integration into building envelopes, which could, enable future developments in the field of energy in buildings, adapted to different and changing environments. In a similar way, such systems could also be used in clothing and in transport vehicles.

7. Conclusion

In conclusion, we reviewed some of the most recent solid-state active thermal devices. In Section 2, we showed the current status of thermal diodes based on their working principle. In Section 3, we presented thermal switches based on their switching mechanism. In Section 4, we reviewed thermal regulators and the different materials that can be used. In Section 5, we reported the recent advances in the development of electrochemical thermal transistors. Finally, in Section 6, we presented an overview of future key aspects of this field.

Based on this, we can conclude that the performances of solid-state thermal devices are still lower than those found for fluidic or mechanical devices.[12] However, this field is still in its early stages, and recent advances have shown that large improvements can be achieved by using novel materials or structures. Especially interesting is the impact of nanotechnology, which has offered new approaches for the development of efficient thermal devices. These solid-state devices present key advantages, namely, non-

moving parts, scalability, and reliability,[5,6] that make them ideal for developing new thermal technology, like heat logic,[9–11] or new thermal management capabilities.[7,8] Additionally, these thermal control devices could contribute to our sustainable energy transition, due to their potential use in energy reduction or scavenging systems.[2] Finally, new parameters could be used to better determine the performance of our thermal control devices. As an example, an energy efficiency parameter $\left(\varepsilon_{\text{switch}} = \dfrac{\dot{Q}_{\text{on}}}{\dot{Q}_{\text{off}} + P} \right)$, defined as the ratio of the heat flux in the on state $\dot{Q}_{\text{on}}$ versus heat flux in the off state $\dot{Q}_{\text{off}}$ plus the power supply P required to switch the operation, could be an important indicator to evaluate the efficiency of a thermal switching process.

Conflict of Interest

The authors declare no conflict of interest.

Keywords

[1] C. Dames, *J. Heat Transfer* **2009**, *131*, 061301.
[2] G. Wehmeyer, T. Yabuki, C. Monachon, J. Wu, C. Dames, *Appl. Phys. Rev.* **2017**, *4*, 041304.
[3] B. Li, L. Wang, G. Casati, *Appl. Phys. Lett.* **2006**, *88*, 143501.
[4] S. Narayana, Y. Sato, *Phys. Rev. Lett.* **2012**, *108*, 214303.
[5] Intel, *No Moving Parts: The Promise of Solid-State Drives*, Intel Visual Adrenalin **2009**, Issue No. 4.
[6] C. Y. Tso, C. Y. H. Chao, *Int. J. Heat Mass Transfer* **2016**, *93*, 605.
[7] C. Alaoui, *IEEE Trans. Veh. Technol.* **2013**, *62*, 98.
[8] C. Acar, I. Dincer, *Energy Storage* **2019**, *1*, e47.
[9] L. Wang, B. Li, *Phys. Rev. Lett.* **2007**, *99*, 177208.
[10] L. Wang, B. Li, *Phys. Rev. Lett.* **2008**, *101*, 267203.
[11] S. R. Sklan, *AIP Adv.* **2015**, *5*, 053302.
[12] K. Klinar, T. Swoboda, M. Muñoz-Rojo, A. Kitanovski **2020**, unpublished.
[13] T. Luo, G. Chen, *Phys. Chem. Chem. Phys.* **2013**, *15*, 3389.

**ADVANCED
SCIENCE NEWS**
www.advancedsciencenews.com

**ADVANCED
ELECTRONIC
MATERIALS**
www.advelectronicmat.de

[14] M. Nomura, J. Shiomi, T. Shiga, R. Anufriev, *Jpn. J. Appl. Phys.* **2018**, *57*, 80101.

[15] D. Vasileska, K. Raleva, S. M. Goodnick, *J. Comput. Electron.* **2008**, *7*, 66.

[16] Q. Liang, Y. L. He, Y. P. Zhou, T. Xie, *Energy Proc.* **2017**, *105*, 4915.

[17] Y. Hasegawa, M. Murata, D. Nakamura, T. Komine, *J. Appl. Phys.* **2009**, *106*, 063703.

[18] G. Xie, Y. Guo, X. Wei, K. Zhang, L. Sun, J. Zhong, G. Zhang, Y. W. Zhang, *Appl. Phys. Lett.* **2014**, *104*, 233901.

[19] K. A. Brucker, J. Majdalani, *Int. J. Heat Mass Transfer* **2005**, *48*, 4779.

[20] J. Chen, G. Zhang, B. Li, *J. Chem. Phys.* **2011**, *135*, 204705.

[21] A. Fallahi, G. Guldentops, M. Tao, S. Granados-Focil, S. Van Dessel, *Appl. Therm. Eng.* **2017**, *127*, 1427.

[22] G. C. Loh, D. Baillargeat, *J. Appl. Phys.* **2014**, *115*, 243501.

[23] Z. Cheng, B. M. Foley, T. Bougher, L. Yates, B. A. Cola, S. Graham, *J. Appl. Phys.* **2018**, *123*, 095114.

[24] A. Ghanekar, Y. Tian, M. Ricci, S. Zhang, O. Gregory, Y. Zheng, *Opt. Express* **2018**, *26*, A209.

[25] Z. Chen, C. Wong, S. Lubner, S. Yee, J. Miller, W. Jang, C. Hardin, A. Fong, J. E. Garay, C. Dames, *Nat. Commun.* **2014**, *5*, 5446.

[26] H. Liu, H. Wang, X. Zhang, *Appl. Sci.* **2019**, *9*, 344.

[27] C. Starr, *J. Appl. Phys.* **1936**, *7*, 15.

[28] C. W. Chang, D. Okawa, A. Majumdar, A. Zettl, *Science* **2006**, *314*, 1121.

[29] N. A. Roberts, D. G. Walker, *Int. J. Therm. Sci.* **2011**, *50*, 648.

[30] Alto University, Heat Flow Control for Future Nanoelectronics, https://phys.org/news/2012-08-future-nanoelectronics.html (accessed: March 2020).

[31] G. Zhang, H. Zhang, *Nanoscale* **2011**, *3*, 4604.

[32] J. Cheh, H. Zhao, *J. Stat. Mech. Theory Exp.* **2012**, *2012*, P06011.

[33] A. Jeżowski, J. Rafalowicz, *Phys. Status Solidi* **1978**, *47*, 229.

[34] H. Wang, S. Hu, K. Takahashi, X. Zhang, H. Takamatsu, J. Chen, *Nat. Commun.* **2017**, *8*, 15843.

[35] W. Kobayashi, Y. Teraoka, I. Terasaki, *Appl. Phys. Lett.* **2009**, *95*, 171905.

[36] Y. Yang, H. Chen, H. Wang, N. Li, L. Zhang, *Phys. Rev. E* **2018**, *98*, 042131.

[37] T. Majdi, S. Pal, I. K. Puri, *Int. J. Therm. Sci.* **2017**, *117*, 260.

[38] X. Sun, S. Kotake, Y. Suzuki, M. Senoo, *Heat Transfer* **2001**, *30*, 164.

[39] V. Kuryliuk, A. Nadtochiy, O. Korotchenkov, C. C. Wang, P. W. Li, *Phys. Chem. Chem. Phys.* **2015**, *17*, 13429.

[40] P. Kim, L. Shi, A. Majumdar, P. L. McEuen, *Phys. Rev. Lett.* **2001**, *87*, 215502.

[41] G. A. Slack, R. A. Tanzilli, R. O. Pohl, J. W. Vandersande, *J. Phys. Chem. Solids* **1987**, *48*, 641.

[42] C. J. Glassbrenner, G. A. Slack, *Phys. Rev.* **1964**, *134*, A1058.

[43] E. Pop, V. Varshney, A. K. Roy, *MRS Bull.* **2012**, *37*, 1273.

[44] R. C. Zeller, R. O. Pohl, *Phys. Rev. B* **1971**, *4*, 2029.

[45] T. M. Tritt, *Thermal Conductivity: Theory, Properties, and Applications*, Physics of Solids and Liquids, Springer, Berlin **2004**.

[46] S. H. Simon, The Oxford Solid State Basics, Oxford **2013**.

[47] A. Amith, I. Kudman, E. F. Steigmeier, *Phys. Rev.* **1965**, *138*, A1270.

[48] J. Callaway, *Phys. Rev.* **1959**, *113*, 1046.

[49] J. A. Leon-Gil, J. J. Martinez-Flores, J. Alvarez-Quintana, *J. Mater. Sci.* **2019**, *54*, 3211.

[50] M. Omini, A. Sparavigna, *Phys. Rev. B* **2000**, *61*, 6677.

[51] C. Uher, *Cryogenics* **1980**, *20*, 445.

[52] D. Sawaki, W. Kobayashi, Y. Moritomo, I. Terasaki, *Appl. Phys. Lett.* **2011**, *98*, 081915.

[53] K. Hirata, T. Matsunaga, S. Singh, M. Matsunami, T. Takeuchi, *J. Electron. Mater.* **2020**, *49*, 2895.

[54] S. O. Kasali, J. Ordonez-Miranda, K. Joulain, *Int. J. Therm. Sci.* **2020**, *153*, 106393.

[55] H. Kang, F. Yang, J. Urban, *Phys. Rev. Appl.* **2018**, *10*, 024034.

[56] W. Kobayashi, D. Sawaki, T. Omura, T. Katsufuji, Y. Moritomo, I. Terasaki, *Appl. Phys. Express* **2012**, *5*, 027302.

[57] D. W. Oh, C. Ko, S. Ramanathan, D. G. Cahill, *Appl. Phys. Lett.* **2010**, *96*, 151906.

[58] H. Kizuka, T. Yagi, J. Jia, Y. Yamashita, S. Nakamura, N. Taketoshi, Y. Shigesato, *Jpn. J. Appl. Phys.* **2015**, *54*, 053201.

[59] A. Fiorino, D. Thompson, L. Zhu, R. Mittapally, S.-A. Biehs, O. Bezencenet, N. El-Bondry, S. Bansropun, P. Ben-Abdallah, E. Meyhofer, P. Reddy, *ACS Nano* **2018**, *12*, 5774.

[60] K. Ito, K. Nishikawa, H. Iizuka, H. Toshiyoshi, *Appl. Phys. Lett.* **2014**, *105*, 253503.

[61] A. Kinaci, M. Kado, D. Rosenmann, C. Ling, G. Zhu, D. Banerjee, M. K. Y. Chan, *Appl. Phys. Lett.* **2015**, *107*, 262108.

[62] V. Eyert, *Ann. Phys.* **2002**, *11*, 650.

[63] M. M. Qazilbash, M. Brehm, G. O. Andreev, A. Frenzel, P. C. Ho, B. G. Chae, B. J. Kim, S. J. Yun, H. T. Kim, A. V. Balatsky, O. G. Shpyrko, M. B. Maple, F. Keilmann, D. N. Basov, *Phys. Rev. B: Condens. Matter Mater. Phys.* **2009**, *79*, 075107.

[64] S. Gražulis, A. Merkys, A. Vaitkus, M. Okulič-Kazarinas, *J. Appl. Crystallogr.* **2015**, *48*, 85.

[65] A. Merkys, A. Vaitkus, J. Butkus, M. Okulič-Kazarinas, V. Kairys, S. Gražulis, *J. Appl. Crystallogr.* **2016**, *49*, 292.

[66] S. Gražulis, D. Chateigner, R. T. Downs, A. F. T. Yokochi, M. Quirós, L. Lutterotti, E. Manakova, J. Butkus, P. Moeck, A. Le Bail, *J. Appl. Crystallogr.* **2009**, *42*, 726.

[67] S. Gražulis, A. Daškevič, A. Merkys, D. Chateigner, L. Lutterotti, M. Quirós, N. R. Serebryanaya, P. Moeck, R. T. Downs, A. Le Bail, *Nucleic Acids Res.* **2012**, *40*, 420.

[68] R. T. Downs, M. Hall-Wallace, *Am. Mineral.* **2003**, *88*, 247.

[69] M. Quirós, S. Gražulis, S. Girdzijauskaitė, A. Merkys, A. Vaitkus, *J. Cheminf.* **2018**, *10*, 23.

[70] J. Ordonez-Miranda, J. M. Hill, K. Joulain, Y. Ezzahri, J. Drevillon, *J. Appl. Phys.* **2018**, *123*, 085102.

[71] A. Kiswandhi, J. Ma, J. S. Brooks, H. D. Zhou, *Phys. Rev. B* **2014**, *90*, 155132.

[72] K. I. Garcia-Garcia, J. Alvarez-Quintana, *Int. J. Therm. Sci.* **2014**, *81*, 76.

[73] B. Song, A. Fiorino, E. Meyhofer, P. Reddy, *AIP Adv.* **2015**, *5*, 053503.

[74] M. Modest, *Radiative Heat Transfer*, Academic, San Diego, CA **2003**.

[75] S. Shen, A. Mavrokefalos, P. Sambegoro, G. Chen, *Appl. Phys. Lett.* **2012**, *100*, 233114.

[76] T. Zhang, T. Luo, *Small* **2015**, *11*, 4657.

[77] K. Joulain, Y. Ezzahri, J. Drevillon, B. Rousseau, D. De Sousa Meneses, *Opt. Express* **2015**, *23*, A1388.

[78] L. P. Wang, Z. M. Zhang, *Nanoscale Microscale Thermophys. Eng.* **2013**, *17*, 337.

[79] J. J. Martinez-Flores, D. Varshney, J. Alvarez-Quintana, *Appl. Phys. Lett.* **2018**, *113*, 264102.

[80] N. A. Roberts, D. G. Walker, *J. Heat Transfer* **2011**, *133*, 092401.

[81] N. A. Roberts, D. G. Walker, *11th Intersoc. Conf. Therm. Thermomech. Phenom. Electron. Syst.* **2008**, *2008*, 993.

[82] X. Cartoixà, L. Colombo, R. Rurali, *Nano Lett.* **2015**, *15*, 8255.

[83] C. M. Bhandari, D. M. Rowe, *J. Phys. C: Solid State Phys.* **1978**, *11*, 1787.

[84] D. G. Cahill, W. K. Ford, K. E. Goodson, G. D. Mahan, A. Majumdar, H. J. Maris, R. Merlin, S. R. Phillpot, *J. Appl. Phys.* **2003**, *93*, 793.

[85] D. Li, Y. Wu, R. Fan, P. Yang, A. Majumdar, *Appl. Phys. Lett.* **2003**, *83*, 3186.

[86] J. J. Ma, J. J. Zheng, W. D. Li, D. H. Wang, B. T. Wang, *Phys. Chem. Chem. Phys.* **2020**, *22*, 5832.

[87] R. J. Mehta, Y. Zhang, C. Karthik, B. Singh, R. W. Siegel, T. Borca-Tasciuc, G. Ramanath, *Nat. Mater.* **2012**, *11*, 233.

**ADVANCED
SCIENCE NEWS**
www.advancedsciencenews.com

**ADVANCED
ELECTRONIC
MATERIALS**
www.advelectronicmat.de

[88] A. Sood, J. Cho, K. D. Hobart, T. I. Feygelson, B. B. Pate, M. Asheghi, D. G. Cahill, K. E. Goodson, *J. Appl. Phys.* **2016**, *119*, 175103.

[89] J. W. Lawson, M. S. Daw, T. H. Squire, C. W. Bauschlicher, *J. Am. Ceram. Soc.* **2012**, *95*, 3971.

[90] G. Pernot, M. Stoffel, I. Savic, F. Pezzoli, P. Chen, G. Savelli, A. Jacquot, J. Schumann, U. Denker, I. Mönch, C. Deneke, O. G. Schmidt, J. M. Rampnoux, S. Wang, M. Plissonnier, A. Rastelli, S. Dilhaire, N. Mingo, *Nat. Mater.* **2010**, *9*, 491.

[91] Z. Yu, L. Ferrer-Argemi, J. Lee, *J. Appl. Phys.* **2017**, *122*, 244305.

[92] K. Sakuma, A. Okada, H. Kawamoto, *J. Mater. Synth. Process.* **1998**, *6*, 315.

[93] E. Pop, *Nano Res.* **2010**, *3*, 147.

[94] J. K. Yu, S. Mitrovic, D. Tham, J. Varghese, J. R. Heath, *Nat. Nanotechnol.* **2010**, *5*, 718.

[95] N. Li, J. Ren, L. Wang, G. Zhang, P. Hänggi, B. Li, *Rev. Mod. Phys.* **2012**, *84*, 1046.

[96] G. Wu, B. Li, *Phys. Rev. B: Condens. Matter Mater. Phys.* **2007**, *76*, 085424.

[97] N. Yang, G. Zhang, B. Li, *Appl. Phys. Lett.* **2008**, *93*, 243111.

[98] N. Yang, G. Zhang, B. Li, *Appl. Phys. Lett.* **2009**, *95*, 033107.

[99] J. W. Jiang, J. S. Wang, B. Li, *EPL* **2010**, *89*, 46005.

[100] D. L. Nika, A. A. Balandin, *J. Phys. Condens. Matter* **2012**, *24*, 233203.

[101] W. Zhao, Y. Wang, Z. Wu, W. Wang, K. Bi, Z. Liang, J. Yang, Y. Chen, Z. Xu, Z. Ni, *Sci. Rep.* **2015**, *5*, 11962.

[102] Y. Wang, A. Vallabhaneni, J. Hu, B. Qiu, Y. P. Chen, X. Ruan, *Nano Lett.* **2014**, *14*, 592.

[103] J. Zhu, S. Shen, K. Hippalgaonkar, K. Wang, Y. Abate, S. Lee, J. Wu, X. Yin, A. Majumdar, X. Zhang, *Nano Lett.* **2014**, *14*, 4867.

[104] H. Tian, D. Xie, Y. Yang, T. L. Ren, G. Zhang, Y. F. Wang, C. J. Zhou, P. G. Peng, L. G. Wang, L. T. Liu, *Sci. Rep.* **2012**, *2*, 523.

[105] X. Shen, X. Lin, J. Jia, Z. Wang, Z. Li, J. K. Kim, *Carbon* **2014**, *80*, 235.

[106] M. M. Rojo, Z. Li, C. Sievers, A. C. Bornstein, E. Yalon, S. Deshmukh, S. Vaziri, M. H. Bae, F. Xiong, D. Donadio, E. Pop, *2D Mater.* **2019**, *6*, 011005.

[107] W. R. Zhong, W. H. Huang, X. R. Deng, B. Q. Ai, *Appl. Phys. Lett.* **2011**, *99*, 193104.

[108] X. Yang, D. Yu, B. Cao, A. C. To, *ACS Appl. Mater. Interfaces* **2017**, *9*, 29.

[109] X. Yang, J. Xu, S. Wu, D. Yu, B. Cao, *J. Phys. Condens. Matter* **2018**, *30*, 435305.

[110] X. Yang, D. Yu, B. Cao, *ACS Appl. Mater. Interfaces* **2017**, *9*, 24078.

[111] J. Lee, V. Varshney, A. K. Roy, J. B. Ferguson, B. L. Farmer, *Nano Lett.* **2012**, *12*, 3491.

[112] X. Yang, J. Xu, S. Wu, D. Yu, B. Cao, *Mater. Lett.* **2019**, *234*, 357.

[113] H. Ma, Z. Tian, *Nano Lett.* **2017**, *18*, 43.

[114] I. Carlomagno, V. A. Cimmelli, D. Jou, *Mech. Res. Commun.* **2020**, *103*, 103472.

[115] K. Takahashi, M. Inoue, Y. Ito, *Jpn. J. Appl. Phys.* **2010**, *49*, 02BD12.

[116] M. Schmotz, J. Maier, E. Scheer, P. Leiderer, *New J. Phys.* **2011**, *13*, 113027.

[117] J. Guo, B. Yang, Y. Yang, X. Yuan, D. Ge, T. Li, P. Yang, *Compos. Interfaces* **2019**, *26*, 127.

[118] P. Yang, X. Li, H. Yang, X. Wang, Y. Tang, X. Yuan, *Appl. Phys. A: Mater. Sci. Process.* **2013**, *112*, 759.

[119] A. Nobakht, Y. Gandomi, J. Wang, M. H. Bowman, D. C. Marable, B. E. Garrison, D. Kim, S. Shin, *Carbon* **2018**, *132*, 565.

[120] J. Bartlett, G. Hardy, I. Hepburn, R. Ray, S. Weatherstone, *Cryogenics* **2010**, *50*, 647.

[121] X. Gou, H. Ping, Q. Ou, S. Qing, H. Xiao, *Appl. Energy* **2015**, *160*, 843.

[122] Y. Utaka, K. Hu, Z. Chen, Y. Zhao, *Appl. Therm. Eng.* **2019**, *155*, 196.

[123] K. Klinar, A. Kitanovski, *Renewable Sustainable Energy Rev.* **2020**, *118*, 109571.

[124] M. A. Beasley, R. L. Edwards, S. L. Firebaugh, A. C. Keeney, R. Osiander, *Proc. SPIE* **2004**, *5344*, 98.

[125] C. Liu, Y. Chen, C. Dames, *Phys. Rev. Appl.* **2019**, *11*, 044002.

[126] B. M. Foley, M. Wallace, J. T. Gaskins, E. A. Paisley, R. L. Johnson-Wilke, J. W. Kim, P. J. Ryan, S. Trolier-Mckinstry, P. E. Hopkins, J. F. Ihlefeld, *ACS Appl. Mater. Interfaces* **2018**, *10*, 25493.

[127] J. F. Ihlefeld, B. M. Foley, D. A. Scrymgeour, J. R. Michael, B. Mckenzie, D. L. Medlin, M. Wallace, S. Trolier-Mckinstry, P. E. Hopkins, *Nano Lett.* **2015**, *15*, 1791.

[128] J. J. Wang, Y. Wang, J. F. Ihlefeld, P. E. Hopkins, L. Q. Chen, *Acta Mater.* **2016**, *111*, 220.

[129] S. Yiğen, A. R. Champagne, *Nano Lett.* **2014**, *14*, 289.

[130] H. Demiryont, D. Moorehead, *Sol. Energy Mater. Sol. Cells* **2009**, *93*, 2075.

[131] H. Demiryont, K. Shannon, R. Ponnappan, *AIP Conf. Proc.* **2006**, *813*, 64.

[132] R. J. Mortimer, *Chem. Soc. Rev.* **1997**, *26*, 147.

[133] J. Matovic, A. Vujanic, C. Kment, K. Reichenberger, *WIT Trans. Ecol. Environ.* **2003**, *73*, 614.

[134] J. Kim, G. K. Ong, Y. Wang, G. Leblanc, T. E. Williams, T. M. Mattox, B. A. Helms, D. J. Milliron, *Nano Lett.* **2015**, *15*, 5574.

[135] D. T. Gillaspie, R. C. Tenent, A. C. Dillon, *J. Mater. Chem.* **2010**, *20*, 9585.

[136] G. Garcia, R. Buonsanti, E. L. Runnerstrom, R. J. Mendelsberg, A. Llordes, A. Anders, T. J. Richardson, D. J. Milliron, *Nano Lett.* **2011**, *11*, 4415.

[137] Y. Wang, E. L. Runnerstrom, D. J. Milliron, *Annu. Rev. Chem. Biomol. Eng.* **2016**, *7*, 283.

[138] P. M. Beaujuge, J. R. Reynolds, *Chem. Rev.* **2010**, *110*, 268.

[139] J. A. Seijas-Bellido, C. Escorihuela-Sayalero, M. Royo, M. P. Ljungberg, J. C. Wojdeł, J. Íñiguez, R. Rurali, *Phys. Rev. B* **2017**, *96*, 140101.

[140] C. Liu, V. Mishra, Y. Chen, C. Dames, *Adv. Theory Simul.* **2018**, *1*, 1800098.

[141] X. Zhao, J. C. Wu, Z. Y. Zhao, Z. Z. He, J. D. Song, J. Y. Zhao, X. G. Liu, X. F. Sun, X. G. Li, *Appl. Phys. Lett.* **2016**, *108*, 242405.

[142] J. Bartlett, G. Hardy, I. D. Hepburn, C. Brockley-Blatt, P. Coker, E. Crofts, B. Winter, S. Milward, R. Stafford-Allen, M. Brownhill, J. Reed, M. Linder, N. Rando, *Cryogenics* **2010**, *50*, 582.

[143] M. J. Dipirro, P. J. Shirron, *Cryogenics* **2014**, *62*, 172.

[144] Z. Y. Zhao, X. G. Liu, Z. Z. He, X. M. Wang, C. Fan, W. P. Ke, Q. J. Li, L. M. Chen, X. Zhao, X. F. Sun, *Phys. Rev. B: Condens. Matter Mater. Phys.* **2012**, *85*, 134412.

[145] J. J. Martínez-Flores, L. Licea-Jimenez, S. A. Perez Garcia, J. Alvarez-Quintana, *J. Appl. Phys.* **2013**, *114*, 104904.

[146] R. Jin, Y. Onose, Y. Tokura, D. Mandrus, P. Dai, B. C. Sales, *Phys. Rev. Lett.* **2003**, *91*, 146601.

[147] C. Hess, B. Büchner, U. Ammerahl, L. Colonescu, F. Heidrich-Meisner, W. Brenig, A. Revcolevschi, *Phys. Rev. Lett.* **2003**, *90*, 197002.

[148] C. Kittel, *J. Phys. Radium* **1959**, *20*, 145.

[149] H. T. Huang, M. F. Lai, Y. F. Hou, Z. H. Wei, *Nano Lett.* **2015**, *15*, 2773.

[150] J. Kimling, R. B. Wilson, K. Rott, J. Kimling, G. Reiss, D. G. Cahill, *Phys. Rev. B: Condens. Matter Mater. Phys.* **2015**, *91*, 144405.

[151] S. Dhara, H. S. Solanki, A. R. Pawan, V. Singh, S. Sengupta, B. A. Chalke, A. Dhar, M. Gokhale, A. Bhattacharya, M. M. Deshmukh, *Phys. Rev. B* **2011**, *84*, 121307.

[152] I. Latella, P. Ben-Abdallah, *Phys. Rev. Lett.* **2017**, *118*, 173902.

[153] A. V. Talyzin, O. Andersson, B. Sundqvist, A. Kurnosov, L. Dubrovinsky, *J. Solid State Chem.* **2007**, *180*, 510.

[154] C. McGuire, K. Sawchuk, A. Kavner, *J. Appl. Phys.* **2018**, *124*, 115902.

[155] Y. Zeng, C.-L. Lo, S. Zhang, Z. Chen, A. Marconnet, *Carbon* **2020**, *158*, 63.

[156] X. Liu, G. Zhang, Y. W. Zhang, *Nano Res.* **2015**, *8*, 2755.

[157] Y. Gao, Q. Liu, B. Xu, *ACS Nano* **2016**, *10*, 5431.

[158] H. S. Kim, J. Jang, J. Yu, S. Y. Kim, *Composites, Part B* **2015**, *79*, 505.

[159] H. Ma, E. O'Donnel, Z. Tian, *Nanoscale* **2018**, *10*, 13924.

[160] M. M. Rojo, J. Martín, S. Grauby, T. Borca-Tasciuc, S. Dilhaire, M. Martin-Gonzalez, *Nanoscale* **2014**, *6*, 7858.

[161] X. Xu, J. Chen, J. Zhou, B. Li, *Adv. Mater.* **2018**, *30*, 1705544.

[162] J. Shin, J. Sung, M. Kang, X. Xie, B. Lee, K. M. Lee, T. J. White, C. Leal, N. R. Sottos, P. V. Braun, D. G. Cahill, *Proc. Natl. Acad. Sci. USA* **2019**, *116*, 5973.

[163] J. Shin, M. Kang, T. Tsai, C. Leal, P. V. Braun, D. G. Cahill, *ACS Macro Lett.* **2016**, *5*, 955.

[164] A. H. Sahraoui, S. Delenclos, S. Longuemart, D. Dadarlat, *J. Appl. Phys.* **2011**, *110*, 033510.

[165] A. R. McLanahan, C. D. Richards, R. F. Richards, *J. Micromechanics Microengineering* **2011**, *21*, 104009.

[166] G. Cha, Y. S. Ju, L. A. Ahuré, N. M. Wereley, *J. Appl. Phys.* **2010**, *107*, 09B505.

[167] T. Yang, B. Kwon, P. B. Weisensee, J. G. Kang, X. Li, P. Braun, N. Miljkovic, W. P. King, *Appl. Phys. Lett.* **2018**, *112*, 063505.

[168] B. Traipattanakul, C. Y. Tso, C. Y. H. Chao, *Int. J. Heat Mass Transfer* **2019**, *135*, 294.

[169] W. Biter, S. Oh, S. Hess, *AIP Conf. Proc.* **2002**, *608*, 73.

[170] A. Ueno, Y. Suzuki, *Int. J. Therm. Sci.* **2018**, *132*, 161.

[171] M. Almanza, L. Depreux, F. Parrain, M. Lobue, *Appl. Phys. Lett.* **2018**, *112*, 083901.

[172] Q. Zheng, G. Zhu, Z. Diao, D. Banerjee, D. G. Cahill, *Adv. Eng. Mater.* **2019**, *21*, 1801342.

[173] R. Xie, C. T. Bui, B. Varghese, Q. Zhang, C. H. Sow, B. Li, J. T. L. Thong, *Adv. Funct. Mater.* **2011**, *21*, 1602.

[174] M. Dietrich, A. Euler, G. Thummes, *Cryogenics* **2014**, *59*, 70.

[175] W. Pfeiler, *Alloy Physics: A Comprehensive Reference*, Wiley-VCH, Wenheim **2007**.

[176] Q. Zheng, S. E. Murray, Z. Diao, A. Bhutani, D. P. Shoemaker, D. G. Cahill, *Phys. Rev. Mater.* **2018**, *2*, 075401.

[177] B. D. Ingale, W. C. Wei, P. C. Chang, Y. K. Kuo, S. K. Wu, *J. Appl. Phys.* **2011**, *110*, 113721.

[178] K. Dahal, Q. Zhang, Y. Wang, I. K. Mishra, Z. Ren, *RSC Adv.* **2017**, *7*, 33775.

[179] T. Zhang, T. Luo, *ACS Nano* **2013**, *7*, 7592.

[180] R. Shrestha, Y. Luan, S. Shin, T. Zhang, X. Luo, J. S. Lundh, W. Gong, M. R. Bockstaller, S. Choi, T. Luo, R. Chen, K. Hippalgaonkar, S. Shen, *Sci. Adv.* **2019**, *5*, eaax3777.

[181] H. Chen, Z. Yue, D. Ren, H. Zeng, T. Wei, K. Zhao, R. Yang, P. Qiu, L. Chen, X. Shi, *Adv. Mater.* **2018**, *31*, 1806518.

[182] B. Feng, J. Tu, J. W. Sun, L. W. Fan, Y. Zeng, *Int. J. Heat Mass Transfer* **2019**, *141*, 789.

[183] C. R. Raj, S. Suresh, R. R. Bhavsar, V. K. Singh, A. S. Reddy, A. Upadhyay, *Mech. Mater.* **2019**, *135*, 88.

[184] H. K. Lyeo, D. G. Cahill, B. S. Lee, J. R. Abelson, M. H. Kwon, K. B. Kim, S. G. Bishop, B. K. Cheong, *Appl. Phys. Lett.* **2006**, *89*, 151904.

[185] J. Lee, E. Bozorg-Grayeli, S. Kim, M. Asheghi, H. S. P. Wong, K. E. Goodson, *Appl. Phys. Lett.* **2013**, *102*, 191911.

[186] W. C. Lo, L. Wang, B. Li, *J. Phys. Soc. Jpn.* **2008**, *77*, 054402.

[187] A. Sood, F. Xiong, S. Chen, H. Wang, D. Selli, J. Zhang, C. J. McClellan, J. Sun, D. Donadio, Y. Cui, E. Pop, K. E. Goodson, *Nat. Commun.* **2018**, *9*, 4510.

[188] A. Myers, How Can We Design Electronic Devices That Don't Overheat, https://engineering.stanford.edu/magazine/article/how-can-we-design-electronic-devices-don-t-overheat (accessed: June 2020).

[189] A. Myers, Researchers Use Thermal Transistor to Protect Electronic Devices from Overheating, https://www.controleng.com/articles/researchers-use-thermal-transistor-to-protect-electronic-devices-from-overheating/ (accessed: June 2020).

[190] L. Wang, B. Li, *Phys. World* **2008**, *21*, 27.

[191] J. Cho, M. D. Losego, H. G. Zhang, H. Kim, J. Zuo, I. Petrov, D. G. Cahill, P. V. Braun, *Nat. Commun.* **2014**, *5*, 4035.

[192] J. S. Kang, M. Ke, Y. Hu, *Nano Lett.* **2017**, *17*, 1431.

[193] J. Sun, H. W. Lee, M. Pasta, H. Yuan, G. Zheng, Y. Sun, Y. Li, Y. Cui, *Nat. Nanotechnol.* **2015**, *10*, 980.

[194] S. Chen, A. Sood, E. Pop, K. E. Goodson, D. Donadio, *2D Mater.* **2019**, *6*, 025033.

[195] T. Tadano, Y. Gohda, S. Tsuneyuki, *Phys. Rev. Lett.* **2015**, *114*, 095501.

[196] G. Zhu, J. Liu, Q. Zheng, R. Zhang, D. Li, D. Banerjee, D. G. Cahill, *Nat. Commun.* **2016**, *7*, 13211.

[197] Q. Lu, S. Huberman, H. Zhang, Q. Song, J. Wang, G. Vardar, A. Hunt, I. Waluyo, G. Chen, B. Yildiz, *Nat. Mater.* **2020**, *19*, 655.

[198] L. Lindsay, D. A. Broido, *J. Phys. Condens. Matter* **2008**, *20*, 165209.

[199] N. Lu, P. Zhang, Q. Zhang, R. Qiao, Q. He, H. B. Li, Y. Wang, J. Guo, D. Zhang, Z. Duan, Z. Li, M. Wang, S. Yang, M. Yan, E. Arenholz, S. Zhou, W. Yang, L. Gu, C. W. Nan, J. Wu, Y. Tokura, P. Yu, *Nature* **2017**, *546*, 124.

[200] K. Klinar, M. M. Rojo, Z. Kutnjak, A. Kitanovski, *J. Appl. Phys.* **2020**, *127*, 234101.

Timm Swoboda received his M.S. degree in Advanced Nanoscience and Nanotechnology from the Autonomous University of Barcelona. He is currently pursuing a Ph.D. degree in the group of Dr. Miguel Muñoz Rojo at the Thermal and Fluid Engineering department of the University of Twente. His research focuses on energy dissipation in electronics and thermal management. His research activities combine both numerical simulations and advanced nanoscale thermal characterization, e.g., scanning thermal microscopy (SThM).

Katja Klinar is a young researcher working in the field of thermal control devices, alternative refrigeration, and heat pump technologies at the Faculty of Mechanical Engineering of the University of Ljubljana, Slovenia. She possesses rich experience in numerical optimization and experimental work related to variety of thermal management problems in household appliances. Her present scientific research activities mainly involve the development of fluidic thermal switches and solid state thermal diodes for applications in systems with cyclical temperature changes, e.g., in caloric energy conversion technologies.

Ananth Yalamarthy is a Staff Engineer at Frore Systems. He has a Bachelor of Technology degree from the Indian Institute of Technology, Madras, India, and a Ph.D. from Stanford University in Mechanical Engineering. His Ph.D. research was at the intersection of energy, electronics, and MEMS devices using wide band gap materials.

Andrej Kitanovski is the head of the research group in the field of refrigeration and heat pumping at the Faculty of Mechanical Engineering, University of Ljubljana. His scientific research activities mainly involve the investigations and development of new caloric energy-conversion technologies and thermal control devices. In 2004, he co-founded the IIR International Magnetic Cooling Working Party that established the well-known IIR Thermag Conferences that presently cover the research and development of caloric technologies worldwide. He is a member of several international associations including IIR, ASHRAE, ASME, MRS, and EHPA.

**ADVANCED
SCIENCE NEWS**
www.advancedsciencenews.com

**ADVANCED
ELECTRONIC
MATERIALS**
www.advelectronicmat.de

Miguel Muñoz Rojo received his Ph.D. degree in condensed matter physics and nanotechnology and his M.S./B.S. degree in physics from the Autonomous University of Madrid. Afterward, he became a postdoctoral researcher at Stanford University. He is currently an assistant professor in the Department of Thermal and Fluid Engineering at the University of Twente. His current research focus is the transport properties of novel 3D, 2D, and 1D materials and their applications in thermal, thermoelectric, and electrical devices.